



Impacts of detrital nano- and micro-scale particles (dNP) on contaminant dynamics in a coal mine AMD treatment system

Liliana Lefticariu ^{a,b,*}, Stephen R. Sutton ^{c,d}, Kelly S. Bender ^e, Mihai Lefticariu ^f, Martin Pentrak ^g, Joseph W. Stucki ^g

^a Department of Geology, Southern Illinois University, Carbondale, IL 62901, USA

^b Environmental Resources and Policy Program, Southern Illinois University, Carbondale, IL 62901, USA

^c Department of Geophysical Sciences, University of Chicago, Chicago, IL 60637, USA

^d Center for Advanced Radiation Sources, University of Chicago, Chicago, IL 60637, USA

^e Department of Microbiology, Southern Illinois University, Carbondale, IL 62901, USA

^f Mass Spectrometry Facility, Southern Illinois University, Carbondale, IL 62901, USA

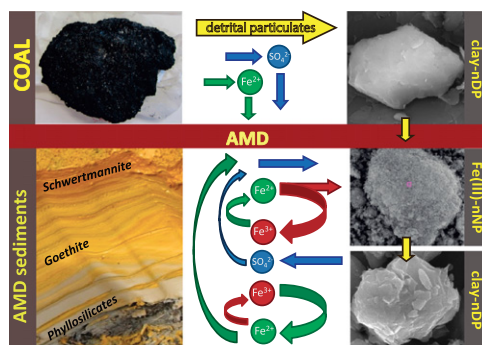
^g Department of Natural Resources and Environmental Sciences, University of Illinois at Urbana-Champaign, Urbana, IL 61801, USA



HIGHLIGHTS

- dNP originated in the coal mine waste were comprised of clay minerals and quartz.
- nNP in the Tab Simco AMD sediments were comprised of schwertmannite and goethite.
- dNP affect Fe and SO₄ sequestration by enhancing heterogeneous nucleation and growth of nNP.
- nNP dissolution in low-permeability areas released Fe and SO₄ back into AMD thus uncoating dNP.
- dNP impacts the overall performance of AMD remediation systems.

GRAPHICAL ABSTRACT



Detrital nano- and micro-scale particles (dNP) originated from the weathering of coal waste represent a significant fraction of coal mine AMD contaminant load and play an important role in both sequestration and remobilization of neofomed nano- and micro-scale particles (nNP).

ARTICLE INFO

Article history:

Received 25 May 2016

Received in revised form 11 September 2016

Accepted 18 September 2016

Available online 17 October 2016

Editor: Simon Pollard

Keywords:

Acid mine drainage

Bioremediation

Nanoparticles

Clay minerals

ABSTRACT

Pollutants in acid mine drainage (AMD) are usually sequestered in **neofomed** nano- and micro-scale particles (nNP) through precipitation, co-precipitation, and sorption. Subsequent biogeochemical processes may control nNP stability and thus long-term contaminant immobilization. Mineralogical, chemical, and microbiological data collected from sediments accumulated over a six-year period in a coal-mine AMD treatment system were used to identify the pathways of contaminant dynamics. We present evidence that **detrital** nano- and micron-scale particles (dNP), composed mostly of clay minerals originating from the partial weathering of coal-mine waste, mediated biogeochemical processes that catalyzed AMD contaminant (1) immobilization by facilitating heterogeneous nucleation and growth of nNP in oxic zones, and (2) remobilization by promoting phase transformation and reductive dissolution of nNP in anoxic zones.

We found that dNP were relatively stable under acidic conditions and estimated a dNP content of ~0.1 g/L in the influent AMD. In the AMD sediments, the initial nNP precipitates were schwertmannite and poorly crystalline

* Corresponding author at: Department of Geology, Southern Illinois University, Carbondale, IL 62901, USA.

E-mail address: lefticar@siu.edu (L. Lefticariu).

Coal mining

Detrital nano-and micro-scale particles (dNP)
Neofomed nano-and micro-scale particles
(nNP)

goethite, which transformed to well-crystallized goethite, the primary nNP repository. Subsequent reductive dissolution of nNP resulted in the remobilization of up to 98% of S and 95% of Fe accompanied by the formation of a compact dNP layer. Effective treatment of pollutants could be enhanced by better understanding the complex, dynamic role dNP play in mediating biogeochemical processes and contaminant dynamics at coal-mine impacted sites.

© 2016 Elsevier B.V. All rights reserved.

1. Introduction

Over the past century, extensive surface and underground coal mining in the Illinois Basin and other regions of the US has left a legacy of a large number of abandoned sites, many of which produce drainages that are acidic and have high contents of S, Fe, Al, and other environmentally relevant pollutants (i.e., As, Cd, Cu, Hg, Ni, Mn, Se, Pb, and Zn) (Cravotta, 2008; Blowes et al., 2014; Lefticariu et al., 2015). Mitigating the environmental impact of acid mine drainages (AMD) is dependent on deciphering the highly complex interplays between the physical and biochemical processes associated with their mobilization, transport, sequestration, and overall long-term fate in natural and engineered systems (Küsel, 2003; Gagliano et al., 2004; Burgos et al., 2012; DiLoreto et al., 2016).

The formation of Fe(III)-rich phases, which in coal mining-impacted areas form a yellow-orange deposit colloquially known as "yellow boy", has been identified as a feasible bioremediation strategy for permanently immobilizing contaminants through precipitation, co-precipitation, sorption, and surface complexation (Waychunas et al., 2005; Hochella et al., 2008; French et al., 2012). These precipitates, typically found as **neofomed** nano- and micro-scale particles (nNP), include amorphous and crystalline phases such as schwertmannite [ideal formula $\text{Fe}_8\text{O}_8(\text{OH})_6\text{SO}_4$; Bigham et al., 1996], goethite ($\alpha\text{-FeOOH}$), lepidocrocite ($\gamma\text{-FeOOH}$), and jarosite [e.g., $\text{KFe}_3(\text{SO}_4)_2(\text{OH})_6$] (Bigham et al., 1996; Caraballo et al., 2013; Yang et al., 2015). The unique properties of nNP, including small size, high surface area, and high reactivity allow them to dominate geochemical processes, even when present in minute amounts (Hochella et al., 2008; Navrotsky et al., 2008).

Microorganisms play key roles in Fe and S cycles in low-pH environments due to their ability to adapt to a remarkable range of extreme conditions (Sánchez-Andrea et al., 2011; Johnson et al., 2012). In AMD-impacted settings, the microbial communities are very active in redox transformation of Fe and as such various microorganisms can catalyze the dissimilatory oxidation of Fe(II) (Fe-oxidizing bacteria-FeOB), or reduction of Fe(III) (Fe-reducing bacteria-FeOB), or can do both depending on the prevailing environmental conditions (Lu et al., 2010; Johnson et al., 2012). Remarkably, the iron-metabolizing acidophiles are highly diverse in low-pH settings, occurring in the domain *Bacteria* within the *Proteobacteria*, *Nitrospirae*, *Firmicutes*, *Actinobacteria*, and *Acidobacteria* phyla, and in the domain *Archaea* within the *Crenarchaeota* and *Euryarchaeota* phyla (Baker and Banfield, 2003; Johnson et al., 2012), and often establish complex interspecies interactions to better cope with harsh acidic conditions (Comolli and Banfield, 2014). At AMD-impacted sites, acidophilic microbial assemblages vary in their response to temperature, organic carbon, pH, and geochemical composition of the mine drainages as well as the local hydrodynamic conditions (Küsel et al., 2008; Burns et al., 2012). Acidophilic FeOB are instrumental in Fe(II) oxidation to Fe(III), which subsequently hydrolyzes and precipitates a wide range of nNP, thus contributing to Fe immobilization (Küsel, 2003; Lu et al., 2013; Lefticariu et al., 2015). Substantial amounts of other AMD contaminants (e.g., heavy metals) are also sequestered by nNP and as such their formation becomes important in controlling pollutants in watershed affected by mining activities (Borch et al., 2009).

Complicating the accurate prediction of contaminant sequestration are the potential transformations of nNP due to both their aforementioned physiochemical properties (Navrotsky et al., 2008) as well as

the strong influence of the redox chemistry and reaction kinetics that control nNP stability (Bigham and Nordstrom, 2000; Waychunas et al., 2005; Braunschweig et al., 2013). These transformations can be both abiotic and biologically-mediated and occur predominantly in systems with fluctuating redox conditions (Küsel et al., 2002; Hansel et al., 2003; Roden, 2012). The microbial-mediated reduction of Fe(III) can comprise both aqueous Fe(III), which has a greater solubility in extremely acidic environments and thus is more bioavailable (Johnson et al., 2012), as well as solid Fe(III) phases (Zachara et al., 2002; Küsel et al., 2002; Hansel et al., 2003).

Recent studies have also shown that **detrital** nano- and micro-scale particles (dNP) can also act as potential vectors of contaminant transport in mining impacted areas (Hudson-Edwards, 2003; Hochella et al., 2005). Especially, many surface water systems have been heavily impacted by the large quantities of dNP released by the active and historic mining activities (Hudson-Edwards, 2016). Increasing attention has been paid to the environmental fate of the metal-bearing dNP originating from mining and mineral processing because they pose a significant environmental threat to organisms, plants, and humans that directly or indirectly interact with contaminated waters (Nordstrom et al., 2015; Hudson-Edwards, 2016).

Most research on contaminant transport and sequestration in coal mining impacted watersheds has focused on dissolved constituents and the formation of nNP (Dold, 2003a; Caraballo et al., 2009; Burgos et al., 2012; Lefticariu et al., 2015) and relatively little research has examined the role of dNP in contaminant transport and particularly on the complex interaction between nNP and dNP in natural systems affected by coal mining. The normal functions of coal mine treatment systems are often impeded by the excessive accumulation of precipitates which can include both nNP and dNP (Lefticariu et al., 2015). Such precipitates can contribute to armoring of the reactive surface areas of the limestone, decreasing permeability and thus affecting the retention time of AMD in the treatment system and consequently reducing the effective lifetime of such engineered system. Therefore, a better understanding of the role of nNP and dNP in the formation of precipitates is critical to understanding the fate and behavior of contaminants in natural systems affected by coal mining as well as for designing more efficient remediation strategies in coal mining impacted areas.

The current study characterizes sediments accumulated over a six-year period in a coal-mine AMD treatment system in Southern Illinois using mineralogical, chemical, and microbiological data. Special attention was given to dNP and their relation to nNP so that mechanisms that control AMD contaminant immobilization and transport in natural and engineered systems can be elucidated. In AMD sediments, the dNP, which were dominated by clay minerals originating from the partial weathering of coal mine waste, played a dominant role in biogeochemical processes that controlled AMD contaminant behavior. Depending on environmental conditions, the dNP promoted either contaminant sequestration as dissolved sulfate and ferric iron precipitate as nNP or remobilization through reductive dissolution of nNP. For the studied AMD system, we provide an estimate of the dNP influx from the coal mine waste. A sequence of plausible biogeochemical redox processes that accounts for both S and Fe sequestration as nNP and S and Fe remobilization during subsequent microbially-mediated transformations is proposed to explain the coal mine contaminant dynamics in the AMD sediments. To our knowledge, this study is the first to report the importance of dNP in contaminant transport in a system impacted by coal mining.

2. Material and methods

2.1. Tab-Simco acid mine drainage treatment system

Tab-Simco site is an abandoned coal mine located approximately 6 km SE of Carbondale, Illinois. The site, recognized as one of the highest contaminated sites in the Midwestern U.S., has been producing persistent contaminated drainage for >40 years, with the AMD containing notably high average concentrations of dissolved inorganic constituents S (60 mM/L), Fe (16 mM/L), Al (7.6 mM/L), Si (1.7 mM/L) and additional environmentally relevant metals (i.e., Mn, V, Cr, Cu, Ni, Zn, Co, and Cd) (Behum et al., 2011; Lefticariu et al., 2015). Two coal seams were mined in the area, namely Murphysboro and Mount Rorah coal members of the Tradewater Formation, which are part of the Pennsylvanian System in the Illinois Basin (Fig. SI-1). Underground coal mining occurred between 1890 and 1955 and was followed by strip mining of both coal seams between 1960 and 1975. The mining activities, which ceased in 1975, left large masses of waste and numerous open underground mine works exposed to weathering. At Tab Simco, the main source of AMD is the acid waters pools formed within the underground mine works. The AMD discharges through a series of seeps into a small tributary that runs north before discharging into the receiving stream, the Sycamore Creek. The reclamation started in 1996 and culminated with the construction of a remediation system designed to treat the coal-generated AMD. The remediation system consists of a sulfate-reducing bioreactor cell (Fig. 1a), two aerobic wetlands, and open limestone drains. The bioreactor cell was lined with an impermeable liner and comprised, from top to bottom, a >0.5-m standing AMD water impoundment, the acid pond (AP), a 2-m thick organic substrate layer

underlying the acid pond, and a 0.3-m limestone layer (Fig. 1b). The organic substrate layer was composed of 53% woodchips, 27% straw mulch, 11% seasoned compost, and 9% agricultural ground limestone. A general description of the study area, the mining history, and the reclamation efforts can be found in our previous reports (Segid, 2010; Behum et al., 2011).

The influent AMD entered the bioreactor cell at one end then infiltrated the organic substrate layer where though a combination of biological and abiotic processes the AMD was treated and subsequently collected within the limestone layer, where perforated 6" PVC pipes and an AgriDrain water control structure were used to discharge the treated effluent AMD (Fig. 1b). An acid pond formed and grew over time due to the slow infiltration rates of the influent AMD into the organic substrate layer. The bioreactor cell was completed in October 2007 and started to treat AMD soon thereafter (Behum et al., 2011). After 6 years of active operation, decreasing AMD remediation efficiency made the replacement of the organic substrate layer within the bioreactor cell necessary. During the years of operation, active precipitation of AMD contaminants occurred in the acid pond and an uneven sediment layer with an average thickness of ~40 cm accumulated on top of the organic substrate layer.

2.2. AMD sediment morphology

Samples were collected from the Tab Simco bioreactor in July 2013 immediately after the AP was drained and the sediments that had been accumulating on top of the organic substrate over a 6 year period were partially exposed. Sediment thickness varied, from ~30 cm at the Tab Simco bioreactor inlet to >50 cm in areas adjacent to the bioreactor

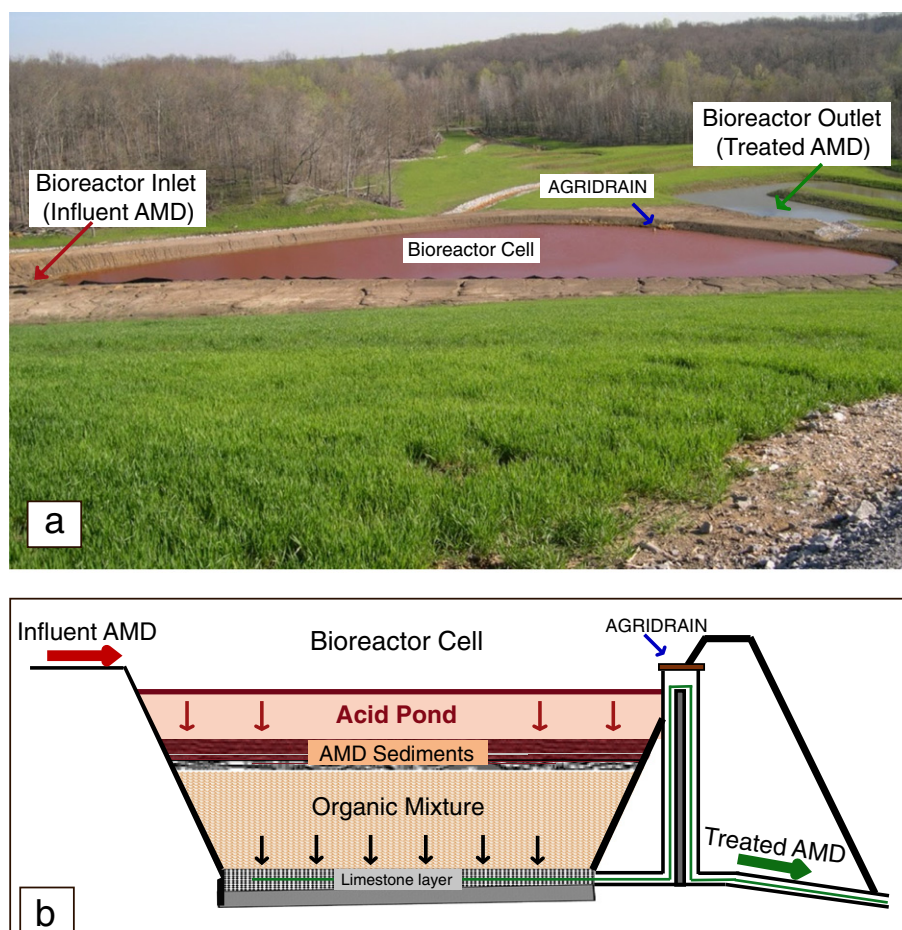


Fig. 1. (a) Overview looking north of the Tab-Simco sulfate-reducing bioreactor treatment system. (b) Cross section view of the Tab-Simco sulfate-reducing bioreactor.

cell outlet (Fig. 2). The top of the sediments formed a highly uneven surface (Fig. 2a), with a topography characterized by depressions (Fig. 2b) and uplifted small mounds (vents) (Fig. 2c, d). Within the OM, the inhomogeneous distribution of bacterial communities resulted in the formation of isolated compartments from which biologically produced gasses were emitted. The upward migration of gasses (i.e., H₂S, CO₂) through the organic substrate layer and the newly formed precipitate layer manifested itself as sediment doming and gas vents with location was marked by gas bubbles at the surface of the acid pond. The vent system provided greater hydrological connectivity between the acid pond and the underlying organic substrate layer, thus potentially increasing the transport of not only gasses out of the organic substrate but also of AMD from the acid pond into the organic substrate layer. The vents were unevenly distributed across the bioreactor with most of them concentrated adjacent to the bioreactor cell outlet. Sediments accumulating on top of this uneven substrate underwent microbially-mediated transformations and developed contrasting hydrological properties, with high-permeability areas (**HPA**) associated with vent systems and low-permeability areas (**LPA**) associated with depressions.

2.3. Sediment core sample collection

Multiple sediment cores were collected in triplicate across the Tab Simco bioreactor at different sampling points using pre-cleaned plastic cylinders that were 7 cm in diameter and ~120 cm in length. Before use, the cylinders were washed with diluted detergent, rinsed with diluted NHO₃ followed by repeated rinses with DI water, and dried at room temperature for 24 h. We examined four sediment cores collected along a transect that stretched from one depression to the top of a proximate vent (Fig. 2a). Immediately after collection, the cores were divided in segments of ~2 cm length and the individual subsamples were

described, weighted, and dried at 50 °C for prompt geochemical and mineralogical analyses, respectively. For pH porewater measurements, immediately after the cores were sectioned, duplicate sediment segments were transferred to 50-mL centrifuge tubes and centrifuged for 30 min at 8000 RCF to separate pore waters from the sediments. The supernatant was collected and the pH and temperature measured using a Hanna® multi-sensor probe using the pH electrode Hanna HI769828-1 field probe (pH/ORP) which was calibrated with Orion pH 1.68, 4.01, and 7.00 buffers and checked against pH 10 buffer.

2.4. Chemical characterization

Quantitative determination of major elements was performed by total dissolution of sediment samples via strong multi-acid digestion and inductively coupled plasma mass spectrometry (ICP-MS) at the AcmeLabs Analytical Laboratories S.A. (Vancouver, Canada). A sample split of 0.25 g was heated in HNO₃-HClO₄-HF to fuming and then dried. The residue was dissolved in HCl and the supernatant analyzed by ICP-MS in low-, medium-, and high-resolution modes, depending on spectral interferences. A mixture of single-element standard solutions (OREAS24P and OREAS24E) was used for instrument calibration. The analytical precision ($\pm 1\sigma$) of standard concentration values was $<\pm 0.05\%$, whereas sample reproducibility was typically $<\pm 0.1\%$. The incomplete digestion of some detrital refractory materials, which we hypothesized might have been present in our samples, could have been only partial and thus the results of the ICM-MS analysis could have been affected. X-ray fluorescence is a physical method that does not suffer from difficulties such as small sample size, incomplete dissolution, matrix effects and sample inhomogeneity found in the acid digestion method. Therefore, duplicate splits were analyzed for (1) bulk concentrations of major oxides (i.e., SiO₂, Fe₂O₃, Al₂O₃) by LiBO₂ fusion

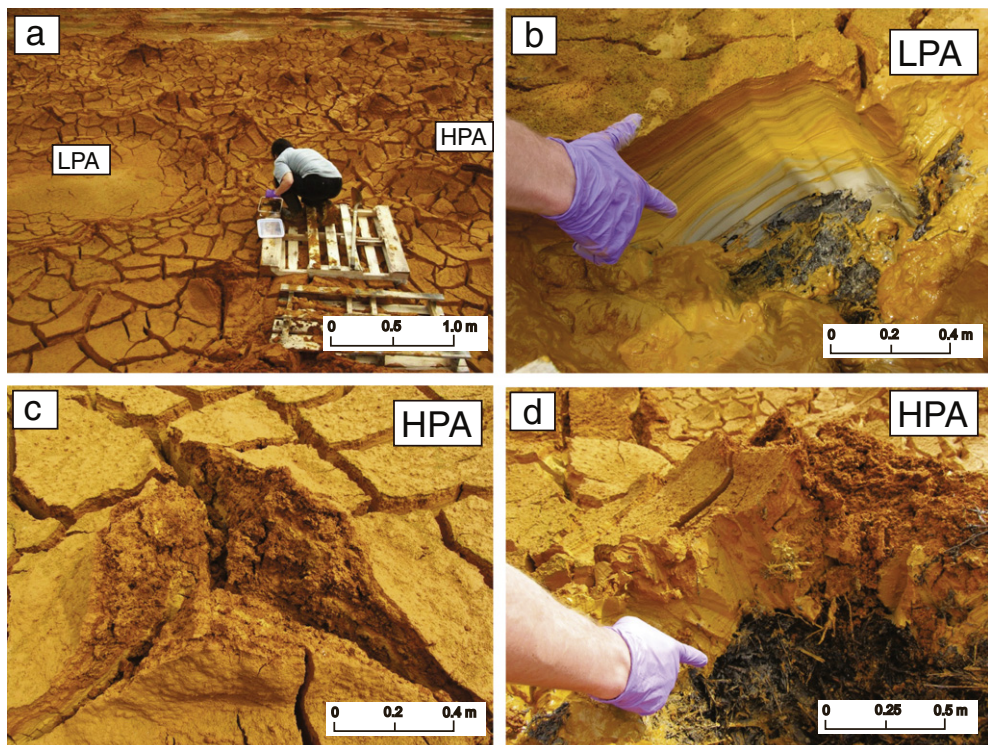


Fig. 2. Overview of the sediment layer accumulated at the Tab Simco passive treatment system within the bioreactor cell over a 6-year period when the TS actively remediated the coalmine AMD. The sediments accumulated on top of the organic substrate matrix underwent microbially-mediated transformations and developed contrasting hydrological properties, with high-permeability areas (**HPA**) associated with vent systems and low-permeability areas (**LPA**) associated with depressions. (b) Close-up view of a LPA where sediments have a striking mineralogical stratification, with an abrupt transition from a goethite-dominated mineralogy in the upper section to a clay minerals-dominated mineralogy in the lower section. (c) Close-up view of a HPA, where the vent system provided greater hydrological connectivity between the acid pond and the underlying organic substrate layer and increased preferential transport of not only gasses out of the OM but also of AMD from the AP into the OM. (d) Close-up view of a HPA, which was characterized by monotonous mineralogy dominated by goethite.

followed by X-ray fluorescence (XRF) spectrometer analysis, and (2) total sulfur (TS) and total carbon (TC) contents were measured by Aqua Regia/ICP-MS analysis also at the AcmeLabs Analytical Laboratories S.A. The measurements were calibrated using the following certified reference materials SY-4(D), OREAS72B, GS311-1, and GS910-4. The analytical precision ($\pm 1\sigma$) of standard concentration values was $<\pm 0.1\%$, whereas sample reproducibility was typically $<\pm 0.2\%$. The detection limit was 0.01% for SiO₂, Fe₂O₃, Al₂O₃ and 0.02% for S. Minimal differences were observed between the ICP-MS and XRF chemical datasets suggesting that refractory minerals, if present, underwent complete dissolution during acid digestion. Therefore, in this study we report the chemical data obtained by acid digestion and inductively coupled plasma mass spectrometer (ICP-MS) analysis.

Total organic carbon (TOC) was determined in dried and acidified sediment samples using a LECO CR - 844 Carbon Analyzer also at the AcmeLabs Analytical Laboratories S.A. Powdered samples were treated with phosphoric acid (1:1) to remove inorganic carbon, dried at 105 °C, and then combusted in an oxygen-rich environment; any carbon present was converted to CO₂ that was carried into a non-dispersive infrared (NDIR) detection cell where the mass of CO₂ was measured by infrared spectrophotometer analysis. The mass was converted to percent total organic carbon based on the dry sample weight.

2.5. Acid ammonium oxalate (AAO) extraction

Duplicate dried AMD sediment samples were also subject to acid ammonium oxalate (AAO) extraction. During AAO extraction procedure, poorly-crystalline ferric and aluminum oxyhydroxysulfate phases, such as schwertmannite, hydrobasaluminite, and gibbsite, are dissolved by acid ammonium oxalate (Dold, 2003a, 2003b; Gagliano et al., 2004; Caraballo et al., 2009). In the case of complex Fe(III) mineral assemblages, only the poorly-crystalline goethite is dissolved during AAO, while well-crystallized goethite particles remain in solid form (Kumpulainen et al., 2007; Peretyazhko et al., 2009).

For the AAO extraction, a 50 mg sediment sample was mixed with ammonium oxalate solution (28 g/L ammonium oxalate ((NH₄)₂C₂O₄) + 15 g/L oxalic acid (H₂C₂O₄) solution, pH ~2.7; Peretyazhko et al., 2009). The mixtures were then shaken in the dark for 4 h, then centrifuged (3000 rpm, 10 min) and filtered (<0.22 µm). The filtered supernatant solutions were analyzed by inductively coupled plasma mass spectrometer (ICP-MS), as previously described.

2.6. Mineralogical characterization

AMD sediments were characterized for their mineralogy using XRD, SEM, and FTIR analysis. XRD patterns were collected at Southern Illinois University in Carbondale (SIUC) using a Rigaku Ultima IV X-ray diffractometer with CuK α radiation. Diffractometer settings were: 40 kV, 30 mA, and a scan range of 2–65° 2 θ , 0.05° 2 θ step size, and 20 s counting time per step. Bulk mineralogical data was collected on randomly oriented powders (e.g., Srodon et al., 2001; Moore and Reynolds, 1997). The identification of mineral phases was made both by utilizing the Jade 9.1, RockJock program and by comparing calculated d-spacing values with published crystal structure data. Selected samples were examined with a FEI Nova NanoSEM 430 field emission scanning electron microscope (SEM) fitted with backscattered and secondary electron detectors, coupled with an energy dispersive spectrometry (EDS) used for semi-quantitative compositional analyses at the IMAGE Facility, Southern Illinois University.

The FTIR spectroscopy in the middle infrared (MIR) region (4000 cm⁻¹–400 cm⁻¹) was carried out at the University of Illinois at Urbana Champaign with a MIDAC M2000 FTIR spectrometer from MIDAC Corp. (Westfield, Massachusetts, USA) equipped with a DTGS detector. In the transmission mode the KBr pellets technique was used. The sample powders (0.5 mg) were mixed and homogenized with 200 mg of

preheated (at 300 °C for 4 h) KBr powder, and then pressed in the Evacuable Pellet Press for 13 mm pellets, PIKE Technologies up to 109,267 PSI. Prepared pellets were then heated overnight at 150 °C to minimize water content in the samples and KBr. The raw spectra were collected after 128 scans of resolution 2 cm⁻¹ and processed using the OPERANT LLC Essential FTIR software package.

2.7. Synchrotron X-ray analysis

Sediment samples were prepared at Spectrum Petrographic as standard 27 × 46mm Suprasil 2 A quartz glass thin sections. Two samples were chosen, namely sample HPA-S3 as representative for a Fe-rich layer and LPA-S2 as representative for an Si-Al-rich layer. XRF elemental maps and Fe K XANES spectra were collected using the X-ray microprobe at Beamline 13-ID-E (GSECARS) at the Advanced Photon Source (APS), Argonne, IL. A cryogenic, dual-crystal, Si(111) monochromator was used to feed monochromatic, undulator X-rays to a dual KB mirror system which focused the beam to ~1 µm (Sutton et al., 2002). XRF maps were obtained by scanning the sample in 2 µm steps in a grid over 500 × 500 µm and collecting the fluorescence (20 msec dwell time) using a quad Vortex Silicon Drift Detector (SDD). Fe K XANES spectra were obtained by collecting Fe K α intensities (fluorescence mode, 1 s dwell time) as the incident energy was scanned through the absorption edge (7030 to 7360 eV).

2.8. Microbiological analysis

DNA was extracted at Southern Illinois University from soil core sections (stored at -20 °C) using the PowerSoil® DNA Isolation Kit (MO BIO Laboratories, Inc.). All sequence processing and analysis steps were performed using the QIIME software package (Caporaso et al., 2010). Sequence libraries were split by core ID and filtered to remove sequence reads of low quality or of length <150 nucleotides. Sequence data was denoised using Denoiser with default parameters within the QIIME environment (Reeder and Knight, 2010). Operational taxonomic units (OTUs) were determined at 97% sequence identity and picked using uclust with default parameters (Edgar 2011). The PyNAST algorithm (Caporaso et al., 2010) was used to align reads against the Greengenes Core reference alignment (DeSantis et al., 2006). Taxonomy was assigned using the default RDP-II classifier function from within QIIME (Wang 2007). Chimera detection was performed using ChimeraSlayer with default parameters (Haas et al., 2011). A phylogenetic tree containing OTUs from all cores was constructed within QIIME using the default method FastTree 2 (Price et al., 2010).

The OTU table containing OTUs for all cores was filtered by fractional abundance less than 0.01 to obtain a list containing the most abundant OTUs. This list was then used to map OTUs to sequence reads using a taxonomic ID table to obtain a list of the fourteen most common representative sequences across all cores. Iteratively rarefied OTU tables were generated using the standard QIIME pipeline and used to compute average Chao1 and Shannon alpha-diversity metrics for each core sampled. Core sample tables rarefied to an even depth of 3910 samples were used to compute distances matrices using the weighted Unifrac method (Lozupone and Knight 2005). UPGMA hierarchical clustering was used to generate a similarity tree containing all sampled and sequenced cores and jackknife support was determined for each node using the default QIIME pipeline.

2.9. Statistical interpretation

The study of the statistical distribution of variables listed in Table SI-2 and the possible correlations among them (Table SI-2) was performed with STATGRAPHICS Centurion XVI.I - × 64 statistical software.

3. Results and discussion

3.1. Sediment chemistry and mineralogy

The examination of *in situ* sediments in multiple cores revealed contrasting geochemical and mineralogical characteristics in HPA and LPA. The HPA sediments displayed relatively uniform major element concentrations, TOC, porewater pH, and sediment water content (Fig. 3a; Table SI-1). In HPA-C1 core there were relatively small vertical variations of Fe_{TOT} ($\text{Fe}_{\text{avg}} = 10,035 \text{ mM/Kg}$; $1\sigma = \pm 573 \text{ mM/Kg}$), which was the primary component, S_{TOT} below 5 cm ($\text{S}_{\text{avg}} = 847 \text{ mM/Kg}$; $1\sigma = \pm 176 \text{ mM/Kg}$), Si_{TOT} ($\text{Si}_{\text{avg}} = 426 \text{ mM/Kg}$; $1\sigma = \pm 259 \text{ mM/Kg}$), and Al_{TOT} ($\text{Al}_{\text{avg}} = 181 \text{ mM/Kg}$; $1\sigma = \pm 109 \text{ mM/Kg}$) concentrations (Table SI-1). We found an inverse correlation between the Fe_{TOT} and Al_{TOT} concentrations, and no significant statistical relationship between pH and the major element concentrations (Table SI-2). This chemistry corresponded to a mineralogy dominated by goethite and schwertmannite, the latter identified mostly in the upper (0–5 cm) sediment layer (Fig. 3a). FTIR spectra of HPA-C1 sediment samples in the MIR region revealed a similar chemical composition of the entire sediment profile. In the region 3900 cm^{-1} – 2700 cm^{-1} the stretching (ν) vibrations of Fe—OH groups related to minerals goethite and schwertmannite were observed (Fig. 3a). Region 1800 cm^{-1} – 1500 cm^{-1} provided the small band near 1650 cm^{-1} attributed to bending (δ) vibration of water molecules (Madejová and Komadel, 2001). The stretching S—O bands attributed to schwertmannite were found in 1300 cm^{-1} – 950 cm^{-1} region, whereas the bending mode of S—O

group was located near 610 cm^{-1} (Boily et al., 2010). The goethite presence was confirmed by a couple of bending OH vibrations $\delta(\text{OH})$ and $\gamma(\text{OH})$ at 892 cm^{-1} and 797 cm^{-1} , respectively (Farmer, 1974).

Unlike HPA-C1, the sediments from LPA-C4 showed, unexpectedly, a downcore increase in the concentrations of Si_{TOT} (from 1900 to 10,080 mM/Kg), Al_{TOT} (from 790 to 2800 mM/Kg), and porewater pH (from 2.3 to 6.2) and a decrease in the concentrations of Fe_{TOT} (from 8000 to 600 mM/Kg), S_{TOT} (from 650 to 35 mM/Kg) and sediment water content (from 82 to 31%) (Fig. 3b). For LPA-C4, significant correlations were found between pH values on one hand and Fe_{TOT} ($r = -0.94$, $p < 0.0001$), S_{TOT} ($r = -0.88$, $p < 0.0001$), Al_{TOT} ($r = +0.95$, $p < 0.0001$), and Si_{TOT} ($r = +0.97$, $p < 0.0001$) on the other hand as well as among the major element concentrations (Table SI-2). The contrasting downcore gradients of Fe—S and Al—Si dominated chemistry corresponded to a striking mineralogical stratification, with an abrupt transition from a goethite-dominated mineralogy in the upper section to clay mineral- and quartz-dominated mineralogy in the lower section (Fig. 3b). This phenomenon was confirmed also by FTIR spectroscopy; increasing concentrations of Al and Si were identified by enlarging of stretching and bending vibrations of Si—O and OH group related to kaolinite, illite, and quartz (Fig. 3b). Decreasing or absence of $\nu(\text{Fe—OH})$, $\delta(\text{Fe—OH})$, $\nu(\text{S—O})$ and $\delta(\text{S—O})$ vibrations was caused by the lower Fe and S contents and the diminishing contribution of goethite to the FTIR spectra.

At the microscale, XRF elemental maps of AMD sediments provided more insight into the complex spatial distribution of selected chemical elements in samples representative of HPA and LPA (Fig. 4). Based on

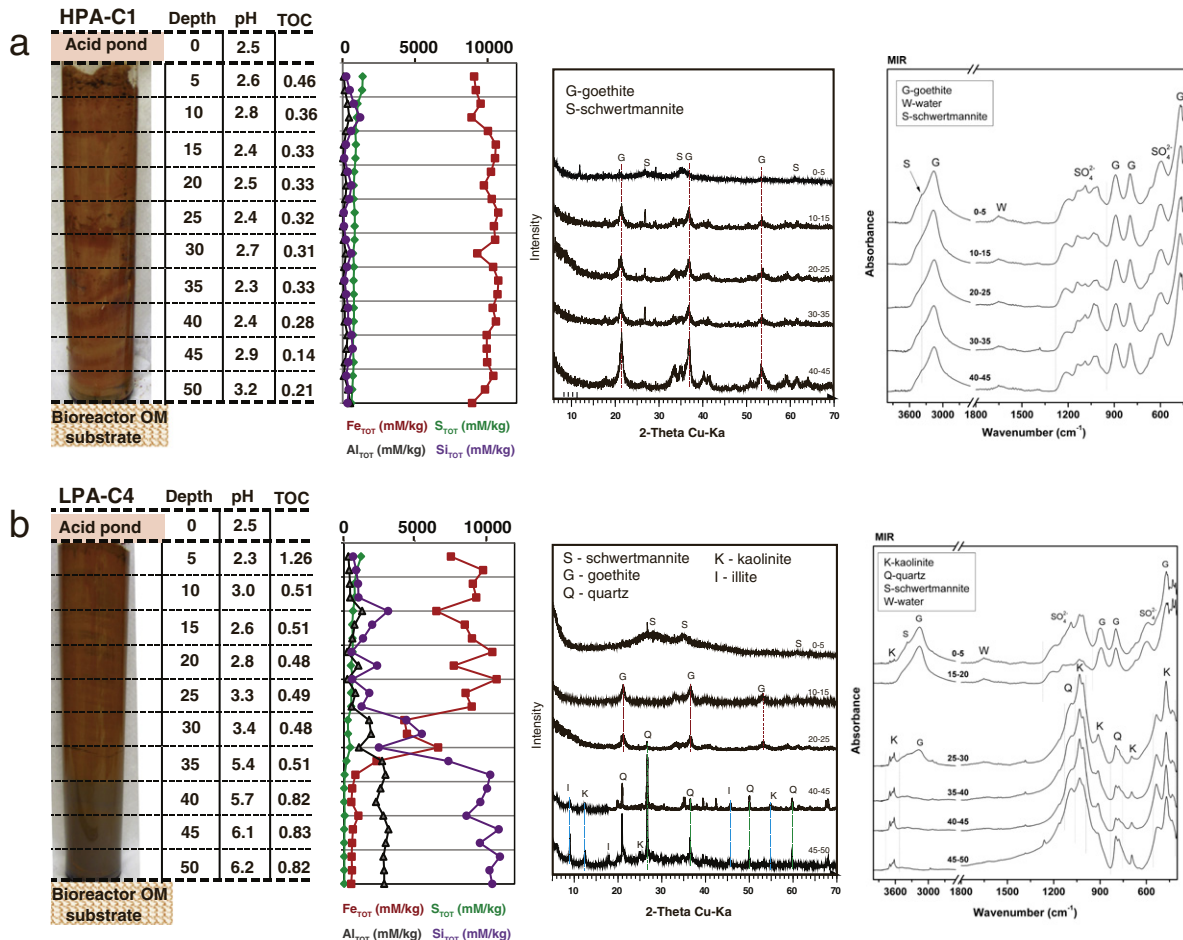


Fig. 3. Geochemical and mineralogical depth profiles in two cores collected from a AMD sediment layer accumulated on top of the Tab Simco bioreactor cell over a 6-year period. (a) Core HPA-C1 was collected from a high-permeability area (HPA) and (b) core LPA-C4 was collected from a low-permeability area (LPA). Details are described in Section S1 of the Supporting Information. Chemical data presented includes porewater pH, sediment TOC, and the total Fe, S, Al, and Si concentrations in AMD sediments. Mineralogical data include XRD and FTIR patterns of untreated AMD sediments.

the expectation that the nNP components of these samples consist of Fe-rich phases (i.e., schwertmannite, goethite, lepidocrocite, and/or jarosite), Fe was used as an nNP proxy. XRF maps show contrasting spatial distribution of Fe in the two samples. In HPA-S3, Fe is present as alternating bands of high- and low-Fe, while in LPA-S2 Fe is present mostly as randomly-distributed, small-scale, high-Fe spots (Fig. 4). To evaluate the Fe speciation heterogeneity at a small scale, Fe K XANES spectra were collected in high and low Fe bands in HPA-S3 (spots 1 and 2, respectively) as well as in a high-Fe spot in LPA-S2 (Fig. 4). Comparison of Fe K XANES spectra (Fig. 5) shows that all three of these spectra are very similar and indicative of Fe with 3+ valence. This data

suggests that Fe^{2+} -bearing phases, such as green rust, were not present in the AMD samples, and that goethite was probable the main Fe^{3+} mineral repository in both HPA and LPA sediments, result concurrent with the XRD and FTIR analyses.

The direct identification by synchrotron XRF analysis of clay minerals and quartz, which were the main dNP components in our samples, proved to be more challenging. Aluminum, which is the main proxy for clay minerals, was difficult to measure for two reasons: first, the low energy X-rays were highly absorbed in the sample and air path to the detector, and second, the possible strong interference from Si, which was abundant in our samples. Additionally, filtering the detector to reduce

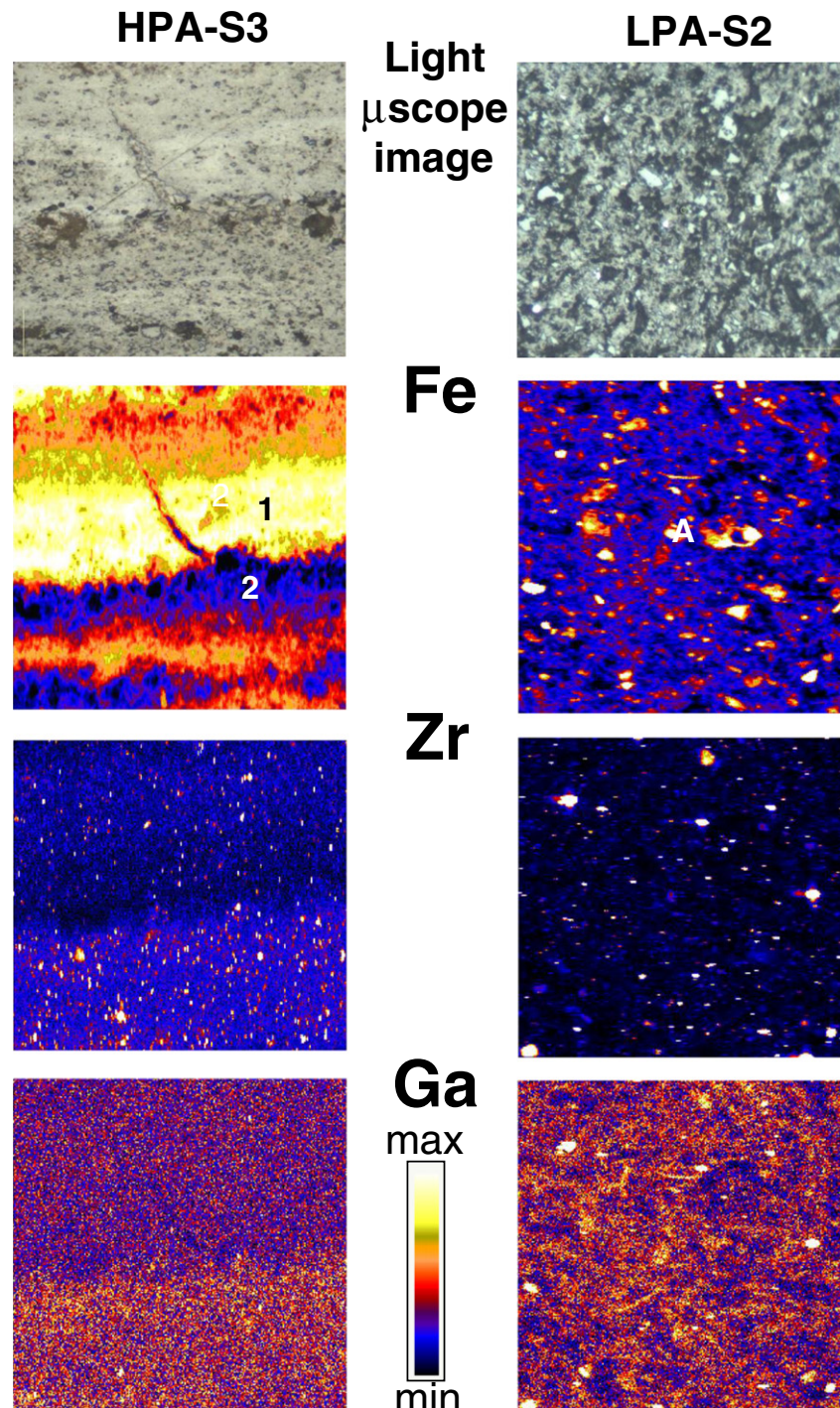


Fig. 4. Images of the LPA-S2 (right) and HPA-S3 (left) samples. Top image are visible light microscope images of the areas chosen for elemental mapping with the XRM. Below those are the XRF maps for Fe, Zr, and Ga. The three labeled locations on the Fe maps were positions where Fe K XANES spectra were collected (see Fig. 3). All images are 500 × 500 μm .

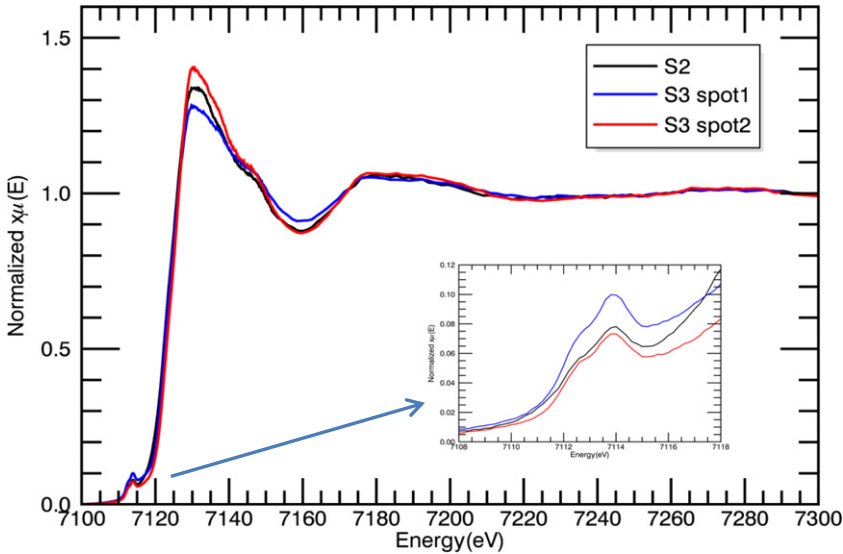


Fig. 5. Fe K XANES spectra for LPA-S2 and two spots (high Fe, low Fe) on the HPA-S3 sample (see analysis locations in Fe maps of Fig. 4). The inset shows the Fe^{3+} dominated pre-edge peak structure.

the Fe fluorescence intensity also prohibited us from seeing Al X-rays. On the other hand, the micro-XRD data provided chemical information sufficient to infer the distribution of detrital Si-Al-rich phases. Our approach was to measure Zr spectra as a proxy for the spatial distribution of detrital minerals and Ga spectra as a proxy for the spatial distribution of clay minerals.

Zirconium maps show dispersed high-Zr hot-spots in both LPA-S2 and HPA-S3. In the AMD sediments, Zr was likely incorporated as zircon (ZrSiO_4), which probably originated in the coal mine waste. Zircon is formed only under extreme temperatures and pressure and at Earth's surface is highly refractory and found as an accessory, detrital mineral ubiquitous in sedimentary rocks (Fedo et al., 2003). The size of the hot-spots in LPA-S2 is relatively larger than in HPA-S3, however in both cases the hot-spots are randomly-distributed within the sediment samples. The presence of these zircon grains supports the existence of a significant detrital component in the AMD sediments.

Because of the similar geochemical character with Al, Ga is commonly found as a trace component in clays and other Si-Al-rich phases (Bradley et al., 1993; Brandt and Kydd, 1998). In clays, Ga^{3+} is incorporated into nonexchangeable framework positions in the phyllosilicate sheets (Brandt and Kydd, 1998) and as such in the present work Ga served as a proxy for clay-dNP. Ga XRF maps show distinct patterns in LPA-S2 and HPA-S3. In HPA-S3, similar to the pattern seen for the Fe XRF map, a layered structure is present where, although the Ga counts are low, there appears to be an inverse correlation between Fe and Ga where the lower Fe region (upper side) has higher Ga (and by inference Al) than the higher Fe region (lower side). In LPA-S2 sample, Ga is rather uniformly distributed, suggesting ubiquitous presence of kaolinite. The hot spots seen in both Ga XRF maps are high Zr grains which produce high background in the Ga region of the XRF spectrum.

3.2. AAO extraction of the AMD sediments

The concentration values of AAO-extracted fractions showed contrasting trends for nNP-associated elements, namely S_{AAO} and Fe_{AAO} , and dNP-associated elements, namely Al_{AAO} and Si_{AAO} . Additionally, for all the elements considered, dissimilar depth profiles for AAO-extracted fractions were mapped in HPA-C1 and LPA-C4 (Fig. 6).

In all AMD sediments, the amount of AAO-extracted sulfur (S_{AAO}) was practically identical to the amount of total S (S_{TOT}) (Fig. 6a, b), with little or no S left in the sediments after AAO extraction. In HPA-C1, S_{AAO} displayed the highest values of 1400 mM/Kg in the uppermost

layer, decreasing downcore to 1000 mM/Kg at ~5 cm, and maintained relative constant downcore concentrations with an average S_{AAO} value of 800 mM/kg (Fig. 6a). Conversely, in LPA-C4, S_{AAO} decreased continuously downcore from 1200 mM/Kg at the top to 30 mM/Kg at 35 cm, a concentration value that characterized the Si-Al-rich layer throughout the bioreactor (Fig. 6b). Since SO_4^{2-} was the only S fraction in the AMD sediments and the concentrations of S_{AAO} and S_{TOT} were analogous in both cores, we infer that SO_4^{2-} was probably associated with either schwertmannite and/or poorly-crystalline goethite, both of which dissolved easily during AAO extractions (Peretyazhko et al., 2009).

In HPA-C1, the amount of AAO extracted iron, Fe_{AAO} , decreased downcore from 8000 mM/kg (~90% of Fe_{TOT}) at the top to 2100 mM/kg (~21% of Fe_{TOT}) at the bottom, in contrast to Fe_{TOT} which exhibited relatively small vertical variations (Fig. 6a). This implies that even though the total amount of Fe-rich phases was relatively constant throughout the core, the ratio of well-crystallized to poorly-crystallized Fe-rich phases increased with depth as a result of dissolution-recrystallization processes (Manceau et al., 2000; Peretyazhko et al., 2009; Caraballo et al., 2013). Comparing the S_{AAO} and Fe_{AAO} downcore trends in HPA-C1, we infer that during transformation of amorphous and poorly-crystalline Fe-rich phases most of the SO_4^{2-} was retained within the AMD sediments, most likely surface-complexed by goethite.

In LPA-C4, two contrasting downcore Fe_{AAO} trends were mapped (Fig. 6b). In the top 20 cm, Fe_{AAO} decreased with depth from 7100 mM/Kg (~94% of Fe_{TOT}) at the top to 1700 mM/Kg (~16% of Fe_{TOT}) at 20 cm, while Fe_{TOT} displayed relatively small variations around an average value of 8860 mM/kg, an overall trend similar to that seen in HPA-C1. Dissimilarly, below a depth of 20 cm, we observed a sudden, parallel drop in both Fe_{TOT} and Fe_{AAO} . The Fe concentration values decreased more than one order of magnitude from $\text{Fe}_{\text{TOT}} = 10,700 \text{ mM/kg}$ and $\text{Fe}_{\text{AAO}} = 1700 \text{ mM/kg}$ at 20 cm to $\text{Fe}_{\text{TOT}} \leq 500 \text{ mM/kg}$ and $\text{Fe}_{\text{AAO}} \leq 70 \text{ mM/kg}$ at a depth of 50 cm. These latter Fe_{TOT} and Fe_{AAO} values were mapped throughout the Si-Al-rich layer of the bioreactor. Overall in LPA-C4, Fe_{AAO} decreased markedly downcore from 7100 mM/kg (~94% of Fe_{TOT}) at the top to 70 mM/kg (~12% of Fe_{TOT}) at 50 cm suggesting that significant mineralogical changes occurred in LPA-C4 during the microbially-mediated transformations.

In the upper layers (0–20 cm), similar to HPA-C1, the mineralogical changes included transformation of schwertmannite and poorly-crystallized goethite to well-crystallized goethite (Fig. 3a, b). For this upper layer, we infer that a higher amount of well-crystallized goethite was present in LPA-C4 since we recorded similar average Fe_{TOT} and S_{TOT}

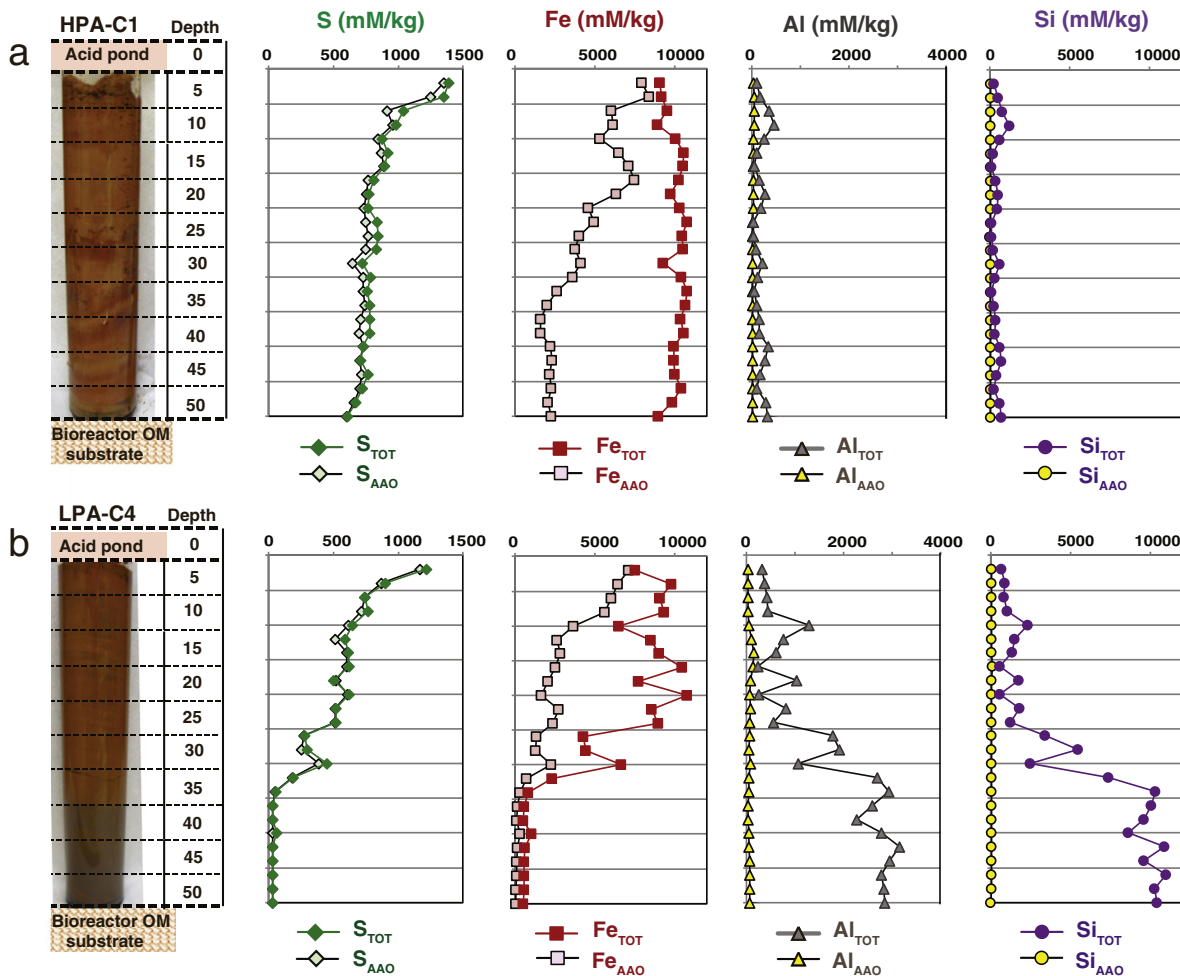


Fig. 6. Geochemical depth profiles of the concentrations for Fe, S, Al, and Si in AMD sediments (TOT) and the solid fraction left after the acid ammonium oxalate extraction (TOT-AAO) in two cores collected from the AMD sediment layer accumulated on top of the Tab Simco bioreactor cell over a 6-year period. (a) Core HPA-C1 was collected from a high-permeability area (HPA) and (b) core LPA-C4 was collected from a low-permeability area (LPA).

values in LPA-C4 and HPA-C1 cores but extracted 39% less Fe_{AAO} and 25% less S_{AAO} in LPA-C4. In the lower layers (20–50 cm), the dramatic decrease in both Fe_{TOT} and Fe_{AAO} indicate that most goethite, regarding of its crystallinity, was dissolved while little or no Fe and SO_4^{2-} retained by the AMD sediments (Fig. 6b).

Conversely, the amount of oxalate extracted aluminum, Al_{AAO} , and silicon, Si_{AAO} , where relatively small with 4% of Al and 1% of Si were extractable in LPA-C4 sediments and 15% of Al and 11% of Si were extractable in HPA-C1 sediments (Fig. 6). The AAO extraction procedure has been shown to dissolve poorly-ordered Al oxide and sulfate precipitates, including Al-bearing minerals such as hydrobasaluminite and gibbsite (Caraballo et al., 2009). In case of our samples the XRD data provided no evidence for the presence of any crystalline or amorphous $\text{Al}(\text{OH})_3$ (Al-hydroxide) phases, thus suggesting that the extracted Al_{AAO} and Si_{AAO} were probably the Al and Si fractions adsorbed and/or incorporated in the AAO-extractable Fe-rich phases (French et al., 2012; Sánchez-España et al., 2016). This hypothesis is also supported by the high molar ratios of $\text{Fe}_{\text{AAO}}/\text{Al}_{\text{AAO}}$ and $\text{Fe}_{\text{AAO}}/\text{Si}_{\text{AAO}}$ with values as high as 230 and 290, respectively, and the SEM-EDS observations which showed the ubiquitous association of Al and Si with Fe-rich phases.

For HPA-C1, we found a significant correlation between S_{AAO} on one hand and Fe_{AAO} ($r = 0.75$, $p < 0.0001$) and Al_{AAO} ($r = 0.74$, $p < 0.0001$) on the other hand and no significant statistical relationship between pH and the main element concentrations (Table SI-2b). For LPA-C4, significant correlations were found between pH values on one hand and

sediment water content (SWC%) ($r = -0.94$, $p < 0.0001$), Fe_{AAO} ($r = -0.76$, $p < 0.0001$), S_{AAO} ($r = -0.88$, $p < 0.0001$), and Si_{AAO} ($r = -0.94$, $p > 0.0001$) on the other hand. Additionally, we found no significant statistical relationship between pH and Al_{AAO} ($r = -0.23$, $p = 0.27$) (Table SI-2b).

3.3. Spatial distribution chemical parameters in AMD sediments

At the field scale, examination of the spatial chemical variability through 2-D profiles extending from a depression to the nearby vent (Fig. 2a) revealed that extensive geochemical heterogeneities and a distinctive layered structure characterized the AMD sediments (Fig. 2b). The contrasting downcore geochemical and mineralogical gradients (Figs. 3, 6) correspond to a layered structure composed of an upper Fe-rich layer with an abrupt transition to a localized, lower Si-Al-rich layer (Fig. 7). These heterogeneities were the result of biogeochemical processes that occurred within the AMD sediments during the 6-year operation of TS bioreactor.

The Fe-rich sediment layer was characterized by low-pH porewater, elevated water contents, high concentrations of Fe_{TOT} and S_{TOT} , and low concentrations of Al_{TOT} and Si_{TOT} (Fig. 7; Table SI-1). The upper (0–5 cm) sediment layer displayed a homogenous composition throughout the bioreactor and had the highest values for S_{TOT} and Fe_{TOT} which can be linked to a mineralogy dominated by schwertmannite and amorphous and poorly-crystalline Fe-rich phases (Fig. 3). Transformation of these initially-precipitated phases occurred readily with the formation of

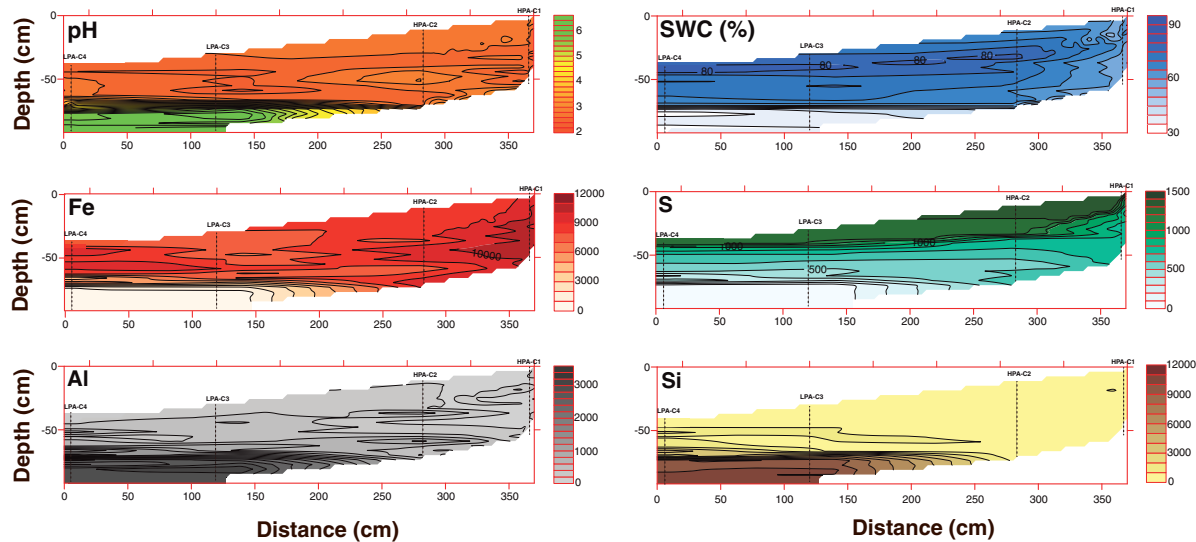


Fig. 7. Contour plots of porewater pH, sediment water content (SWC %), and elemental concentration for Fe, S, Al, and Si in AMD sediments along a 2-D profile [depth from the sediment top (cm) vs. distance between a HPA to the nearby LPA (cm)].

goethite, the main Fe repository in the AMD sediments, which displayed increased crystallinity with depth throughout the Fe-rich layer. Commonly, Fe_{TOT} and Al_{TOT} showed local spatial variations which corresponded to layers with either high goethite/clay mineral ratios (higher Fe concentrations; dark-red color) or low goethite/clay mineral ratios (lower Fe concentrations; light-red color) (Fig. 2b; and HPA-S3 sample in Fig. 4).

Restricted AMD circulation in LPA allowed for more complex transformation to occur within the AMD sediments, which included extensive dissolution of goethite and concentration of dNP in an Si-Al-rich layer (Figs. 3, 4, and 7). The Si-Al-rich sediment layer was characterized by high-pH porewater, relatively low sediment water contents, high concentrations of Al_{TOT} and Si_{TOT} , and negligible concentrations of Fe_{TOT} and S_{TOT} (Fig. 7; Table SI-1). Mineralogically, the Si-Al-rich layer was dominated by the presence of clay minerals and quartz, with minor presence of other dNP (e.g., zircon) (Figs. 3 and 4). Kaolinite and illite were identified in the XRD and FTIR patterns of AMD samples from LPA-C4 lower section (Fig. 3b) with the overall clay abundance proportional to Al_{TOT} . Even though dNP were identified in all AMD sediments (Fig. 4; Section SI-2), LPA contained a higher dNP fraction than HPA (Figs. 3, 4), probably due to restricted AMD circulation in LPA and thus lower dissolution rates for dNP in these areas.

3.4. Biogeochemical controls on precipitation and transformation of nNP

Previous research at Tab Simco has shown that dissolved $\text{Fe}(\text{II})$, resulted from the oxidative dissolution of pyrite in coalmine waste (Lefticariu et al., 2006), was oxidized to ferric iron [$\text{Fe}(\text{III})$] in the acid pond oxic waters either abiotically or by acidophilic iron oxidation microorganisms (FeO) of the class *Betaproteobacteria* and *Alphaproteobacteria* (Burns et al., 2012). The high molar ratio S:Fe of 4:1 in the acid pond assures ample supplies of SO_4^{2-} for reaction and thus the produced $\text{Fe}(\text{III})$ was predominately complexed by SO_4^{2-} and precipitated as schwertmannite, which was the main Fe phase detected by powder XRD and FTIR in the upper sediment layer (Fig. 3). The formation of these precipitates consumes substantial amounts of Fe and SO_4^{2-} and releases protons.

Pyrosequencing of the microbial community present throughout the LPA column indicated that members of the *Gammaproteobacteria*, the uncharacterized *JG37-AG-4*, *Acidimicrobia*, and *Alphaproteobacteria* classes were the most abundant in the AMD sediments (Fig. 8). The top 30 cm of the LPA column, corresponding to the Fe-rich layer, was dominated by bacteria related to the *Gammaproteobacteria* class

(65%, 45%, and 52% of the OTUs in the 10, 20, and 30 cm sections of the column, respectively) (Fig. 8). In the 30–50 cm intervals of the LPA column, corresponding to the Si-Al-rich layer, the abundance of *Gammaproteobacteria* phylotypes decreased significantly (12% and 4% of the detected OTUs, respectively) as abundance increases were detected for other classes. Because members of this bacterial class have been implicated in both acidic Fe oxidation and reduction (Shipeng et al., 2010; Johnson et al., 2012), we predict bacteria corresponding to these sequences are cycling Fe in the acidic sediments. Members of the *Acidimicrobia*, the uncharacterized *JG37-AG-4*, and *Alphaproteobacteria* (most abundant below 30 cm with 22% of the 50 cm OTUs) (Fig. 8) classes have also been implicated in iron cycling reactions in acidic environments (Coupland and Johnson, 2008; García-Moyano et al., 2012; Johnson et al., 2012). Of particular interest are species of *Acidiphilium* (*Alphaproteobacteria*), some of which are capable of reducing the $\text{Fe}(\text{III})$ in schwertmannite (Shipeng et al., 2010). In addition to oxidizing $\text{Fe}(\text{II})$, members of the *Acidimicrobia* class are capable of reducing $\text{Fe}(\text{III})$ under oxygen limiting conditions (Bridge and Johnson, 1998). It should be noted that OTUs corresponding to sulfate-reducing bacteria were not detected in the LPA column (data not shown).

In the AMD sediments, the opposing trends in the geochemical gradients for $\text{Fe}_{\text{TOT}} - \text{S}_{\text{TOT}}$ and $\text{Al}_{\text{TOT}} - \text{Si}_{\text{TOT}}$ (Fig. 3b) as well as in the abundances of microbial communities (Fig. 8) were probably the result of successive microbially-mediated transformations. Schwertmannite, a poorly-crystalline nNP, tends to aggregate and transform to goethite, which is a crystalline, more thermodynamically stable phase (Bigham and Nordstrom, 2000; Gagliano et al., 2004; Cornell and Schwertmann, 2003) with subsequent release of structural and adsorbed SO_4^{2-} back into solution (Rose and Ghazi, 1997; Caraballo et al., 2013). Goethite, the primary $\text{Fe}(\text{III})$ -nNP repository in the AMD sediments (Figs. 3, 6), has low solubility in aqueous solutions (Caraballo et al., 2013) and its overall thermodynamic stability is a function of crystal structure, composition and particle size. Mineralogical changes observed such as schwertmannite transformation to goethite and increased goethite crystallinity with depth may be explained by biologically-mediated Fe cycling processes in the AMD sediments. Significantly, the microbially-mediated mineralogical transformations in the Fe-rich layers seems to be dependent on the local hydrological conditions, with higher ratios of poorly crystallized goethite to well-crystallized goethite found in HPA.

Based on downcore decreasing Fe_{TOT} and Fe_{AAO} concentrations (Fig. 6), Fe minerals occurrence and distribution as revealed by XRD

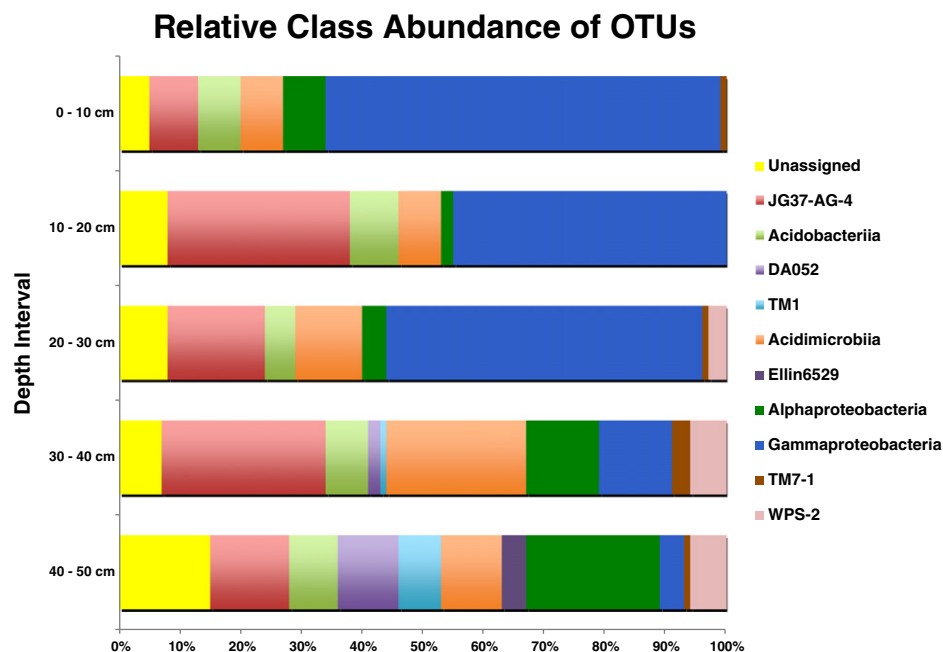


Fig. 8. Relative bacterial class abundance within the LPA column. Abundance in each depth interval was based on OTUs chosen at 97% sequence similarity cutoff.

(Fig. 3), FTIR (Fig. 3), and XRF maps (Fig. 4), as well as the distribution of microbial communities (Fig. 8), we propose that extensive reductive dissolution of goethite took place (Fig. 6 a, b), up to total loss of crystalline Fe-rich phases in the lower section of LPA (Figs. 4; 6b). Various interconnected mechanisms including protonation, complexation, and reduction can contribute to the goethite dissolution. The significant inverse correlation between Fe_{TOT} content and porewater pH in the AMD sediments (Table SI-2) suggests that protonation had a minimum effect on goethite dissolution. Complexation by organic chelates and siderophores (Cheah et al., 2003; Kraemer, 2004), probably abundant in coal-generated AMD, could have increased the dissolution of goethite and the bioavailability of Fe(III) for microbial reduction in porewater. A combination of substitutions and structural defects in goethite crystals (Manceau et al., 2000) can also accelerate dissolution. Reduction of dissolved Fe(III) as well as amorphous and crystalline Fe(III)-nNP can occur both abiologically (e.g., via the redox cycling of humic acids; Lovley et al., 1996) or biologically by the direct enzymatic reduction of Fe(III) oxides to Fe(II) by dissimilatory FeRB (DIRM, Lovley, 1991; Lovley et al., 1993). While in many environments goethite is less energetically suitable as electron acceptor for FeRB, in the AMD sediments, additional H_2 and organic ligands from the underlying organic substrate layer could have provided inorganic electron donors for FeRB (Johnson and Hallberg, 2008). The net reactions for bacterial iron reduction, then, are strongly acid consuming and highly pH-dependent. While current data cannot unequivocally determine the single important mechanisms, we suggest that a combination of abiotic and biological processes together with the development of favorable local conditions resulted in goethite dissolution.

3.5. Role of clay-dNP in AMD contaminant dynamics

Clay-dNP had a profound bearing on biogeochemical processes at the Tab Simco site due their unique properties, which include small size, large surface area, layer charge, and chemical reactivity towards both neutral and charged species as well as microorganisms.

Clay minerals, chiefly kaolinite and illite/smectite, are the main inorganic constituents in coals of Tradewater Formation (Murphyboro and Mt. Rorah coals) and overburden at the Tab Simco site (Fig. 9a), with Al_2O_3 content up to 20 wt% measured in low-temperature ash (Lefticariu, 2009). The progressive weathering of coal and rapid

dissolution of pyrite generates AMD enriched in dissolved Fe , SO_4^{2-} , and heavy metals (Lefticariu, 2009) and leaves behind a residual composed of macerals, clay minerals, and quartz (Fig. 9b).

Under acidic (<2.5) conditions, such as those in the Tab Simco coal mine waste (Segid, 2010), proton-promoted dissolution of clays results in decreased particle size and increased specific surface area, porosity and surface reactivity (Galan et al., 1999; Pentrak et al., 2012). Protons tend to adsorb on exchange sites and replace interlayer cations thus initiating a slow decomposition of the phyllosilicate layers by liberating octahedral cations (Komadel and Madejová, 2006). The extent of clay-acid interaction is controlled by crystal structure and chemical composition (Jozefaciuk and Bowanko, 2002) as well as solution chemistry. In mixed clays, preferential dissolution of smectite (Metz et al., 2005; Vazquez et al., 2011) is often observed over illite (Shaw et al., 2009; Bibi et al., 2011) and kaolinite (Cama et al., 2002; Bibi et al., 2014), the latest being more resistant to acid attack due to restricted access of protons to the interlayer space and preferential dissolution limited to the particle edges.

At Tab Simco, we found that clay-dNP are relatively stable under low-pH conditions both in coal mine AMD and AMD sediments. Additional laboratory analyses of the AMD suspended load samples and AMD sediments treated by CDB (citrate-dithionite-bicarbonate extraction procedure) revealed the omnipresence of clay minerals (Section SI-2). The acid-modified clay-dNP have unique properties (Komadel and Madejová, 2006), including high surface area/volume ratios as well as increased reactivity and catalytic properties, and thus provide a unique framework for interrelated microbial and geochemical processes. Microorganisms, which are often present at or near clay surfaces as these are enriched in ions and organic matter relative to AMD (Kostka et al., 2002; Theng and Orchard, 1995), promoted complex biogeochemical reactions in AMD sediments. Concurrently, bacterial coatings and biofilm formation (Konhauser and Urrutia, 1999; Dong et al., 2009; Vasiliadou et al., 2011; Mueller, 2015), which has been observed in the presence of clay minerals (Maurice et al., 2001a), including smectite (Alimova et al., 2009; Perdrial et al., 2009), could have protected clay surfaces from sustained acid attack and created microniches for optimal microbial processes.

The clay-dNP provided reactive surfaces for heterogeneous nucleation and growth of nNP, especially Fe(III) phases (Fig. 9c) that have very small solubility products at low pH. At TS, this process was

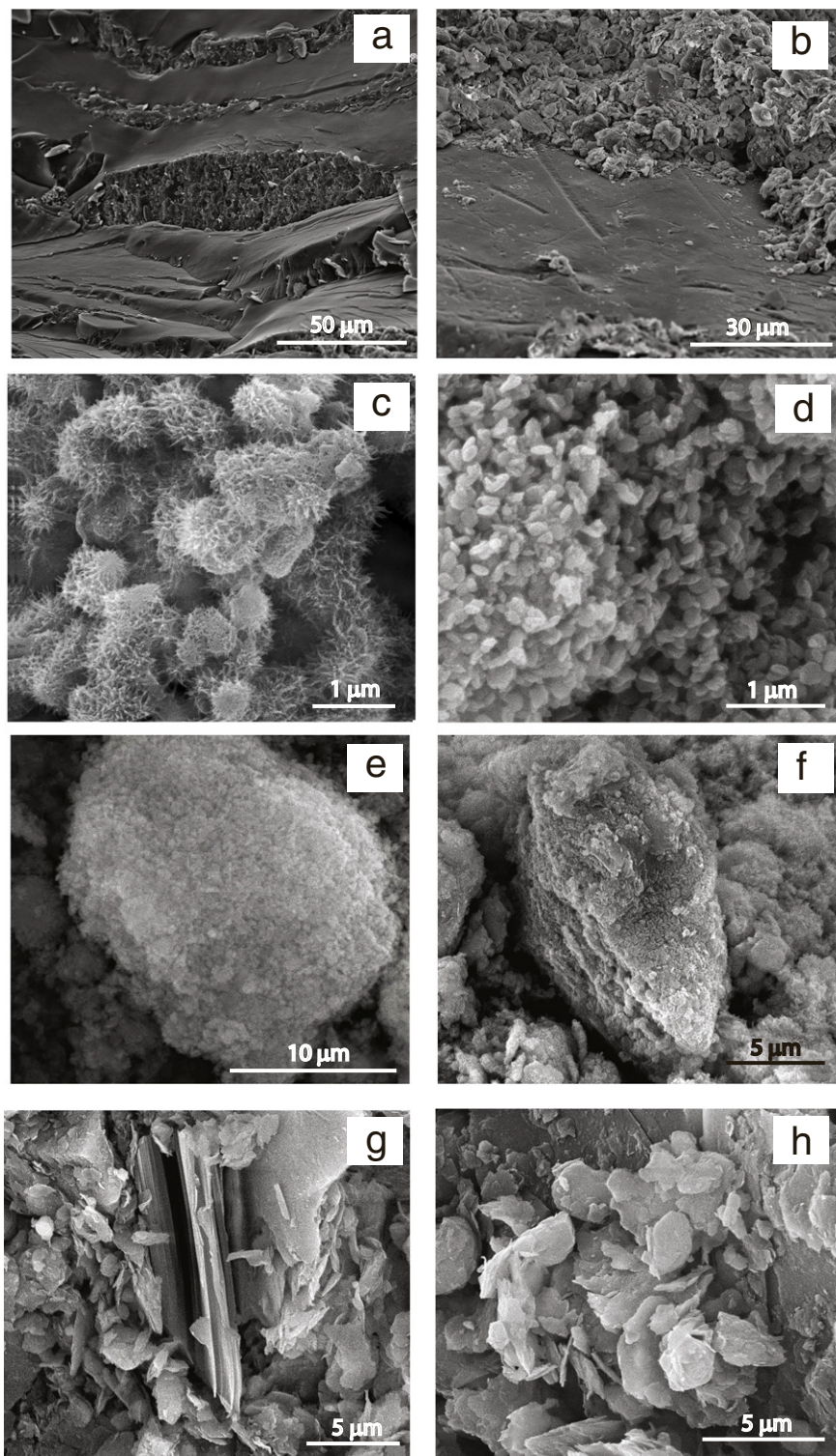


Fig. 9. SEM images of solid components of the Tab-Simco remediation system. (a) Unweathered Murphysboro coal sample containing bands of organic macerals (smooth areas) intermixed with mineral matter dominated by clay minerals (kaolinite). (b) Weathered Murphysboro coal sample showing a residual layer of clay minerals (upper section) and coal macerals (lower section). (c) Schwertmannite, the chief minerals found in the uppermost AMD sediment layer with morphology resembling a coral like structure. (d), (e), and (f) Goethite, the dominant mineral in the Fe-rich layer of the AMD sediments, forms aggregates that completely covered detrital particulates. Formation of these coatings could have further protected detrital particulates for dissolution. (g) and (h) Detrital clay minerals, which in the lower section of Si-Al-rich layer of the AMD sediments are not coated by Fe-precipitates.

extensive since, as showed by XRD, FTIR, SEM data as well as in Fe XRF maps, dNP became totally encrusted within Fe(III)-nNP (Fig. 9 c-f). These Fe(III)-nNP coatings changed the surface reactivity and the *point of zero charge* (PZC) value of dNP and thus further modified the surface retention capacity for AMD pollutants. In the acid pond, increased

particle size and variable charge surfaces of the growing nNP promoted flocculation, settlement, and ultimately the formation of the AMD sediment layer in the Tab Simco bioreactor cell.

In contrast, microbially-mediated processes in the AMD sediments catalyzed by clay-dNP promoted transformation and dissolution of

nNP (Fig. 9 g, h). For example, the dissolution of goethite in the lower LPA (Fig. 6) could have resulted from a positive feedback process enhanced by clay-dNP: dissimilatory bacterial reduction of Fe(III) generated Fe(II) in porewater, which could have either diffused upwards or be adsorbed on goethite surfaces, which in turn accelerated the dissolution of goethite and thus produced more bioavailable Fe(III) for reduction. Partial dissolution of clay-dNP combined with FeRB processes generated porewater alkalinity, which changed local geochemical conditions and further favored FeRB activity (Komadel et al., 2006). This positive feedback was highly efficient only locally in the AMD sediments where AMD influx was restricted, such as in the lower LPA. Sustained AMD influx in the upper Fe-rich sediment layers and throughout HPA assured that any dissolution was balanced by fresh precipitation of Fe(III)-nNP (Figs. 6, 7).

Sediment transformations also comprised decreasing water content (Fig. 7) through mineral dehydration, transformation, and dissolution as well as sediment compaction. Dissolution of nNP favored the formation of a compact, low-permeability dNP layer (Fig. 4) capable of further decreasing AMD flow from the Tab Simco acid pond into the organic substrate layer. Over time, decreased AMD remediation in the bioreactor cell, as observed at Tab Simco, may have been related to the sealing properties of the clay-dNP layer.

3.6. Calculation of the dNP influx at Tab Simco

We estimate an average dNP influx to the Tab Simco bioreactor cell of ~0.1 g/L using an average AMD flow rate of 70 L/min and a total AMD sediment volume of 1210 m³ and assuming that most dNP are concentrated in the Si-Al-rich layer (SI, Section S1). Sediment chemical analysis shows that for every mol of dNP influx, 2–14 mol of S and 7–44 mol of Fe were initially sequestered as nNP. Decreasing S/Fe molar ratios from 4/1 in the AMD influent, to 1/6 in the upper sediment layers, and further to 1/20 in the lower sediment layer point to overall low S sequestration in the AMD sediments. Our results also show that S, which in AMD sediments was predominantly associated with AAO fraction, could be easily remobilized during dissolution-recrystallization processes.

Iron sequestration as nNP in the AMD sediments, initially, was greatly efficient. However, long-term Fe sequestration was dependent on dissimilatory FeRB processes, which in turn were dependent on restricted access of AMD to the AMD sediments. Compared to HPA, increased reductive dissolution of goethite resulted in Fe mobilization with ~50% Fe loss in upper LPA and up to ~95% Fe loss in lower LPA. During the six years of bioreactor operation, we estimate that >90% of S and >50% of Fe, initially sequestered as nNP were remobilized in solution through mineral transformation and dissolution. Work in progress at Tab Simco shows that the mechanisms of promoting sequestration and/or mobilization of the major AMD contaminants (e.g., Fe, S) were also a template for the behavior of trace metals, with major implications for long-term contaminant transport and immobilization in coal mining-impacted watersheds.

4. Conclusions and environmental implications

Our study demonstrates for the first time that dNP inherited from the coal mine wastes can persist in low-pH mine drainages and become a support for biogeochemical processes that control the fate and transport of contaminants in watersheds affected by coal mining. At Tab Simco remediation site, the dNP fraction dominated by clay-minerals and quartz played a fundamental role in AMD contaminant dynamics. The presence of dNP highly enhanced AMD contaminant immobilization by providing support for nNP heterogeneous crystallization followed by precipitation. It is proposed that the AMD sediment started accumulating as quartz- and clay-dNP coated with schwertmannite and poorly-crystalline goethite. Sulfate, the chief dissolved component in coal mine AMD, was initially sequestered either as SO₄-rich nNP

(e.g., schwertmannite) and/or surface-bound to poorly-crystalline goethite. Depending on local hydrological conditions, subsequent transformations of nNP resulted in partial or total SO₄²⁻ remobilization. This result is significant since it shows that SO₄²⁻, which in AMD sediments at Tab Simco was exclusively associated with AAO extractable fraction, can be easily remobilized during subsequent microbially-mediated processes. Iron, which is also a major dissolved contaminant in coal mine AMD, was predominantly sequestered in AMD sediments as Fe(III)-rich nNP (e.g., goethite). However, similar to S, the Fe(III)-rich nNP were subsequently prone to dissolution/recrystallization processes. When the biogeochemical conditions within the AMD sediments started favoring iron reduction, the well-crystallized goethite nNP coatings were dissolved that resulted in partial or total Fe remobilization which left behind a dNP-rich layer dominated by clay-minerals and quartz. Overall, recrystallization and dissolution of nNP greatly contributed to remobilization of coal mine AMD contaminants.

In watersheds affected by coal mining activities both dNP and nNP can contribute in complex and subtle ways not only to local contaminant immobilization but also to long-run contaminant transport since coated dNP may be less affected by dissolution and thus prone to long-distance contaminant transport and dispersion. Promoting the precipitation of Fe(III)-rich nNP in natural and/or engineered system (e.g., engineered wetlands, terraced iron formations), can only be a short-term approach to AMD remediation, since subsequent transformations of the AMD sediments may result in contaminant remobilization. Excessive accumulation of precipitates as unwanted scale and/or layers within different components of a natural watershed and/or AMD remediation system, such was the case of Tab Simco sulfate-reducing bioreactor, can further impede the normal functions of these natural and/or engineered systems. Furthermore, nNP can incorporate toxic elements (e.g., Cd, Cr, Ni, Pb, and Zn) either structurally or adsorbed, so the solubility of nNP may govern the sequestration and transport of contaminants in coal mining impacted sites.

Highlighting the key role that dNP play in contaminant transport and sequestration, could lead not only to better understanding of mechanisms that govern the transport, immobilization and removal of contaminants in watersheds affected by historical and active coal mining activities but also to novel, better technologies for treatment of contaminated drainage associated with coal mining and beyond. Finally, other areas of coal and coal waste utilization, such as the design of bio/geotechnical engineering technologies for metal recovery from mining waste, may benefit from our findings.

Acknowledgements

Funding for this study was provided by the Office of Surface Mining Reclamation and Enforcement (OSM) Applied Science Program Cooperative Agreement S11AC20018 AS. Portions of this work were performed at GeoSoilEnviroCARS (Sector 13), Advanced Photon Source (APS), Argonne National Laboratory. GeoSoilEnviroCARS is supported by the National Science Foundation - Earth Sciences (EAR-1128799) and Department of Energy- Geosciences (DE-FG02-94ER14466). This research used resources of the Advanced Photon Source, a U.S. Department of Energy (DOE) Office of Science User Facility operated for the DOE Office of Science by Argonne National Laboratory under Contract No. DE-AC02-06CH11357. Other portions of this study used resources provided by the Program in Physical Chemistry of Clays, University of Illinois at Urbana-Champaign, which received financial support from the National Science Foundation, under grants EAR 10-53491 and EAR 11-48459; the Department of Navy under contract W9126G-12-2-0027; and the Illinois College of Agricultural, Consumer, and Environmental Sciences Office of Research, Multi-State Project. The two anonymous reviewers and Simon J. Pollard, Associate Editor, are thanked for their comments and suggestions, which improved the quality and clarity of this manuscript.

Appendix A. Supplementary data

Supplementary data to this article can be found online at <http://dx.doi.org/10.1016/j.scitotenv.2016.09.154>.

References

- Alimova, A., Katz, A., Steiner, N., Rudolph, E., Wei, H., Steiner, J.C., Gottlieb, P., 2009. Bacteria-clay interaction: structural changes in smectite induced during biofilm formation. *Clay Clay Miner.* 57, 205–212.
- Baker, B.J., Banfield, J.F., 2003. Microbial communities in acid mine drainage. *FEMS Microbiol. Ecol.* 44 (2), 139–152.
- Behum, P.T., Lefticariu, L., Bender, K.S., Segid, Y.T., Burns, A.S., Pugh, C.W., 2011. Remediation of coal-mine drainage by a sulfate-reducing bioreactor: a case study from the Illinois coal basin, USA. *Appl. Geochem.* 26, S162–S166.
- Bibi, I., Singh, B., Silvester, E., 2011. Dissolution of illite in saline-acidic solutions at 25 °C. *Geochim. Cosmochim. Acta* 75, 323–3249.
- Bibi, I., Singh, B., Silvester, E., 2014. Dissolution kinetics of soil clays in sulfuric acid solutions: ionic strength and temperature effects. *Appl. Geochem.* 51, 170–183.
- Bigham, J.M., Nordstrom, D.K., 2000. Iron and aluminum hydroxysulfates from acid sulfate waters. *Rev. Mineral. Geochem.* 40, 351–403.
- Bigham, J.M., Schwertmann, U., Traina, S.J., Winland, R.L., Wolf, M., 1996. Schwertmannite and the chemical modeling of iron in acid sulfate waters. *Geochim. Cosmochim. Acta* 60, 2111–2121.
- Blowes, D.W., Ptacek, C.J., Jambor, J.L., Weisener, C.G., Paktunc, D., Gould, W.D., Johnson, D.B., 2014. The geochemistry of acid mine drainage. In: Sherwood Lollar, B. (Ed.), Environmental Geochemistry. In: Holland, H.D., Turekian, K.K. (Eds.), Treatise on Geochemistry Vol. 11. Elsevier, pp. 113–190 Exec. Eds.
- Boily, J.-F., Gassman, P.L., Peretyazhko, T., Szanyi, J., Zachara, J.M., 2010. FTIR spectral components of schwertmannite. *Environ. Sci. Technol.* 44, 1185–1190.
- Borch, T., Kretzschmar, R., Kappler, A., Cappellen, P.V., Ginder-Vogel, M., Voegelin, A., Campbell, K., 2009. Biogeochemical redox processes and their impact on contaminant dynamics. *Environ. Sci. Technol.* 44, 15–23.
- Bradley, S.M., Howe, R.F., Kydd, R.A., 1993. Correlation between ^{27}Al and ^{71}Ga NMR chemical shifts. *Magn. Reson. Chem.* 31, 883–886.
- Brandt, K.B., Kydd, R.A., 1998. Gallium and chromium substitution for aluminum in synthesized beidellite. *Clay Clay Miner.* 46, 139–144.
- Braunschweig, J., Bosch, J., Meckenstock, R.U., 2013. Iron oxide nanoparticles in geomicrobiology: from biogeochemistry to bioremediation. *New Biotechnol.* 30, 793–802.
- Bridge, T.A.M., Johnson, D.B., 1998. Reduction of soluble iron and reductive dissolution of ferric iron-containing minerals by moderately thermophilic iron-oxidizing bacteria. *Appl. Environ. Microbiol.* 64 (6), 2181–2186.
- Burgos, W.D., Borch, T., Troyer, L., Luan, F., Larson, L., Brown, J.F., Shimizu, M., 2012. Schwertmannite and Fe oxides formed by biological low-pH Fe (II) oxidation versus abiotic neutralization: impact on trace metal sequestration. *Geochim. Cosmochim. Acta* 76, 29–44.
- Burns, A.S., Pugh, C.W., Segid, Y.T., Behum, P.T., Lefticariu, L., Bender, K.S., 2012. Performance and microbial community dynamics of a sulfate-reducing bioreactor treating coal generated acid mine drainage. *Biodegradation* 23, 415–429.
- Cama, J., Metz, V., Ganor, J., 2002. The effect of pH and temperature on kaolinite dissolution rate under acidic conditions. *Geochim. Cosmochim. Acta* 66, 3913–3926.
- Caporaso, J.G., Kuczynski, J., Stombaugh, J., Bittinger, K., et al., 2010. QIIME allows analysis of high-throughput community sequencing data. *Nat. Methods* 7, 335–336.
- Caraballo, M.A., Rotting, T.S., Nieto, J.M., Ayora, C., 2009. Sequential extraction and DXRD applicability to poorly crystalline Fe- and Al-phase characterization from an acid mine water passive remediation system. *Am. Mineral.* 94, 1029–1038.
- Caraballo, M.A., Rimstidt, J.D., Macías, F., Nieto, J.M., Hochella, M.F., 2013. Metastability, nanocrystallinity and pseudo-solid solution constraints to schwertmannite solubility. *Chem. Geol.* 360/361, 22–31.
- Cheah, S.F., Kraemer, S.M., Cervini-Silva, J., Sposito, G., 2003. Steady-state dissolution kinetics of goethite in the presence of desferrioxamine B and oxalate ligands: implications for the microbial acquisition of iron. *Chem. Geol.* 198, 63–75.
- Comolli, L.R., Banfield, J.F., 2014. Inter-species interconnections in acid mine drainage microbial communities. *Front. Microbiol.* 5, 367.
- Cornell, R.M., Schwertmann, U., 2003. The Iron Oxides: Structure, Properties, Reactions, Occurrence and Uses. 2nd ed. Wiley VCH Publishers, New York, p. 703.
- Coupland, K., Johnson, D.B., 2008. Evidence that the potential for dissimilatory ferric iron reduction is widespread among acidophilic heterotrophic bacteria. *FEMS Microbiol. Lett.* 279, 30–35.
- Cravotta, C.A.I.I., 2008. Dissolved metals and associated constituents in abandoned coal-mine discharges, Pennsylvania, USA. 1. Constituent concentrations and correlations. *Appl. Geochem.* 23, 166–202.
- DeSantis, T.Z., Hugenholtz, P., Larsen, N., Rojas, M., Brodie, E.L., Keller, K., 2006. Greengenes, a chimera-checked 16S rRNA gene database and workbench compatible with ARB. *Appl. Environ. Microbiol.* 72, 5069–5072.
- DiLoreto, Z.A., Weber, P.A., Weiserer, C.G., 2016. Solid phase characterization and metal deportment in a mussel shell bioreactor for the treatment of AMD, Stockton coal mine, New Zealand. *Appl. Geochem.* 67, 133–143.
- Dold, B., 2003a. Dissolution kinetics of schwertmannite and ferrihydrite in oxidized mine samples and their detection by differential X-ray diffraction (DXRD). *Appl. Geochem.* 18, 1531–1540.
- Dold, B., 2003b. Speciation of the most soluble phases in a sequential extraction procedure adapted for geochemical studies of copper sulfide mine waste. *J. Geochem. Explor.* 80, 55–68.
- Dong, H., Jaisi, D.P., Kim, J., Zhang, G., 2009. Review paper. Microbe-clay mineral interactions. *Am. Mineral.* 94, 1505–1519.
- Edgar, R.C., 2010. Search and clustering orders of magnitude faster than BLAST. *Bioinformatics* 26, 2460–2461.
- Farmer, V.C., 1974. The infrared spectra of minerals. Monograph 4. Mineralogical Society, London (539 pp).
- Fedo, C.M., Sircombe, K.N., Rainbird, R.H., 2003. Detrital zircon analysis of the sedimentary record. *Rev. Mineral. Geochem.* 53 (1), 277–303.
- French, R.A., Caraballo, M.A., Kim, B., Rimstidt, J.D., Murayama, M., Hochella, M.F., 2012. The enigmatic iron oxyhydroxysulfate nanomineral schwertmannite: morphology, structure, and composition. *Am. Mineral.* 97, 1469–1482.
- Gagliano, W.B., Brill, M.R., Bigham, J.M., Jones, F.S., Traina, S.J., 2004. Chemistry and mineralogy of ochreous sediments in a constructed mine drainage wetland. *Geochim. Cosmochim. Acta* 68, 2119–2128.
- Galan, E., Carretero, M.I., Fernandez-Caliani, J.C., 1999. Effects of acid mine drainage on clay minerals suspended in the Tinto River (Rio Tinto, Spain). An experimental approach. *Clay Miner.* 34, 99–112.
- García-Moyano, A., González-Toril, E., Aguilera, A., Amils, R., 2012. Comparative microbial ecology study of the sediments and the water column of the Rio Tinto, an extreme acidic environment. *FEMS Microbiol. Ecol.* 81, 303–314.
- Hansel, C.M., Benner, S.G., Neiss, J., Dohnalkova, A., Kukkadapu, R.K., Fendorf, S., 2003. Secondary mineralization pathways induced by dissimilatory iron reduction of ferrihydrite under advective flow. *Geochim. Cosmochim. Acta* 67, 2977–2992.
- Hochella, M.F., Moore, J.N., Putnis, C., Putnis, A., Kasama, T., Eberl, D.D., 2005. Direct observation of heavy metal-mineral association from the Clark Fork River superfund complex: implications for metal transport and bioavailability. *Geochim. Cosmochim. Acta* 69, 1651–1663.
- Hochella, M.F., Lower, S.K., Maurice, P.A., Penn, R.L., Sahai, N., Sparks, D.L., Twining, B.S., 2008. *Science* 319, 1631–1635.
- Hudson-Edwards, K.A., 2003. Sources, mineralogy, chemistry and fate of heavy metal-bearing particles in mining-affected river systems. *Mineral. Mag.* 67, 205–217.
- Hudson-Edwards, K., 2016. Tackling mine wastes. *Science* 352 (6283), 288–290.
- Johnson, D.B., Hallberg, K.B., 2008. Carbon, iron and sulfur metabolism in acidophilic micro-organisms. *Adv. Microb. Physiol.* 54, 201–255.
- Johnson, D.B., Kanao, T., Hedrich, S., 2012. Redox transformations of iron at extremely low pH: fundamental and applied aspects. *Front. Microbiol.* 3, 96.
- Jozefaciuk, G., Bowanko, G., 2002. Effect of acid and alkali treatments on surface areas and adsorption energies of selected minerals. *Clay Clay Miner.* 50 (6), 771–783.
- Komadel, P., Madejová, J., 2006. Acid activation of clay minerals. In: Bergaya, F., Theng, B.K.G., Lagaly, G. (Eds.), Handbook of Clay Science. Elsevier, Amsterdam, pp. 263–287.
- Komadel, P., Madejová, J., Stucki, J.W., 2006. Structural Fe(III) reduction in smectites. *Appl. Clay Sci.* 34, 88–94.
- Konhauser, K.O., Urrutia, M.M., 1999. Bacterial clay authigenesis: a common biogeochemical process. *Chem. Geol.* 161 (4), 399–413.
- Kostka, J.E., Dalton, D.D., Skelton, H., Dollhopf, S., Stucki, J.W., 2002. Growth of iron (III)-reducing bacteria on clay minerals as the sole electron acceptor and comparison of growth yields on a variety of oxidized iron forms. *Appl. Environ. Microbiol.* 68, 6256–6262.
- Kraemer, S.M., 2004. Iron oxide dissolution and solubility in the presence of siderophores. *Aquat. Sci.* 66, 3–18.
- Kumpulainen, S., Carlson, L., Raisanen, M.L., 2007. Seasonal variations of ochreous precipitates in mine effluents in Finland. *Appl. Geochem.* 22 (4), 760–777.
- Küsel, K., 2003. Microbial cycling of iron and sulfur in acidic coal mining lake sediments. *Water Air Soil Pollut.* 13, 67–90.
- Küsel, K., Roth, U., Drake, H., 2002. Microbial reduction of Fe(III) in the presence of oxygen under low pH conditions. *Environ. Microbiol.* 4, 414–421.
- Küsel, K., Blöthe, M., Schulz, D., Reiche, M., Drake, H.L., 2008. Microbial reduction of iron and porewater biogeochemistry in acidic peatlands. *Biogeoosci. Discuss.* 5 (3), 2165–2196.
- Lefticariu, L., Pratt, L.M., Ripley, E.M., 2006. Mineralogic and sulfur isotopic effects accompanying oxidation of pyrite in millimolar solutions of hydrogen peroxide at temperatures from 4 to 150 °C. *Geochim. Cosmochim. Acta* 70 (19), 4889–4905.
- Lefticariu, L., 2009. Integrated Study of Mercury and Other Trace Elements Distribution in Illinois Coal. Final report to Illinois Clean Coal Institute (44 pp).
- Lefticariu, L., Walters, E.R., Pugh, C.W., Bender, K.S., 2015. Sulfate reducing bioreactor dependence on organic substrates for remediation of coal-generated acid mine drainage: field experiments. *Appl. Geochem.* 63, 70–82.
- Lovley, D.R., 1991. Dissimilatory Fe(III) and Mn(IV) reduction. *Microbiol. Rev.* 55, 259–287.
- Lovley, D.R., Giovannoni, S.J., White, D.C., Champine, J.E., Phillips, E., Gorby, Y.A., Goodwin, S., 1993. *Geobacter metallireducens* gen. nov. sp. nov., a microorganism capable of coupling the complete oxidation of organic compounds to the reduction of iron and other metals. *Arch. Microbiol.* 159, 336–344.

- Lovley, D.R., Coates, J.D., Blunt-Harris, E.L., Phillips, E.J., Woodward, J.C., 1996. Humic substances as electron acceptors for microbial respiration. *Nature* 382, 445–448.
- Lozupone, C., Knight, R., 2005. UniFrac: a new phylogenetic method for comparing microbial communities. *Appl. Environ. Microbiol.* 71, 8228–8235.
- Lu, S., Gischkat, S., Reiche, M., Akob, D.M., Hallberg, K.B., Küsel, K., 2010. Ecophysiology of Fe-cycling bacteria in acidic sediments. *Appl. Environ. Microbiol.* 76, 8174–8183.
- Lu, S., Chourey, K., Reiche, M., Nietzsche, S., Shah, M.B., Neu, T.R., Hettich, R.L., Küsel, K., 2013. Insights into the structure and metabolic function of microbes that shape pelagic iron-rich aggregates (“iron snow”). *Appl. Environ. Microbiol.* 79 (14), 4272–4281.
- Madejová, J., Komadel, P., 2001. Baseline studies of the clay mineral society source clays: infrared methods. *Clay Clay Miner.* 49, 410–432.
- Manceau, A., Schlegel, M.L., Musso, M., Sole, V.A., Gauthier, C., Petit, P.E., Trolard, F., 2000. Crystal chemistry of trace elements in natural and synthetic goethite. *Geochim. Cosmochim. Acta* 64, 3643–3661.
- Maurice, P.A., Vierkorn, M.A., Hersman, L.E., Fulghum, J.E., 2001. Dissolution of well and poorly ordered kaolinites by an aerobic bacterium. *Chem. Geol.* 180, 81–97.
- Metz, V., Amram, K., Ganor, J., 2005. Stoichiometry of smectite dissolution reaction. *Geochim. Cosmochim. Acta* 69, 1755–1767.
- Moore, D.M., Reynolds Jr., R.C., 1997. X-ray Diffraction and the Identification and Analysis of Clay Minerals. Oxford University Press, New York (378 p.).
- Mueller, B., 2015. Experimental interactions between clay minerals and bacteria: a review. *Pedosphere* 25 (6), 799–810.
- Navrotksy, A., Mazeina, L., Majzlan, J., 2008. Size-driven structural and thermodynamic complexity in iron oxides. *Science* 319 (5870), 1635–1638.
- Nordstrom, D.K., Blowes, D.W., Ptacek, C.J., 2015. Hydrogeochemistry and microbiology of mine drainage: an update. *Appl. Geochem.* 57, 3–16.
- Pentrak, M., Címerová, A., Madejová, J., Komadel, P., 2012. Changes in layer charge of clay minerals upon acid treatment as obtained from their interactions with methylene blue. *Appl. Clay Sci.* 55, 100–107.
- Perdrial, J.N., Warr, L.N., Perdrial, N., Lett, M.C., Elsass, F., 2009. Interaction between smectite and bacteria: implications for bentonite as backfill material in the disposal of nuclear waste. *Chem. Geol.* 264, 281–294.
- Peretyazhko, T., Zachara, J.M., Boily, J.F., Xia, Y., Gassman, P.L., Arey, B.W., Burgos, W.D., 2009. Mineralogical transformations controlling acid mine drainage chemistry. *Chem. Geol.* 262, 169–178.
- Price, M.N., Dehal, P.S., Arkın, A.P., 2010. FastTree 2-Approximately Maximum-Likelihood Trees for Large Alignments. *Plos One* 5 (3).
- Roden, E.E., 2012. Microbial iron-redox cycling in subsurface environments. *Biochem. Soc. Trans.* 40, 1249–1256.
- Rose, S., Ghazi, A.M., 1997. Release of sorbed sulfate from iron oxyhydroxides precipitated from acid mine drainage associated with coal mining. *Environ. Sci. Technol.* 31, 2136–2140.
- Sánchez-Andrea, I., Rodriguez, N., Amils, R., Sanz, J.L., 2011. Microbial diversity in anaerobic sediments at Rio Tinto, a naturally acidic environment with a high heavy metal content. *Appl. Environ. Microbiol.* 77, 6058–6093.
- Sánchez-España, J., Yusta, I., Gray, J., Burgos, W.D., 2016. Geochemistry of dissolved aluminum at low pH: extent and significance of Al-Fe (III) coprecipitation below pH 4.0. *Geochim. Cosmochim. Acta* 175, 128–149.
- Segid, Y.T., 2010. Evaluation of the Tab-Simco Acid Mine Drainage Treatment System: Water Chemistry, Performance, and Treatment Processes. Unpubl. M.S. thesis. Southern Illinois Univ., Carbondale.
- Shaw, S.A., Peak, D., Hendry, M.J., 2009. Investigation of acidic dissolution of mixed clays between pH 1.0 and –3.0 using Si and Al X-ray absorption near edge structure. *Geochim. Cosmochim. Acta* 73, 4151–4165.
- Shipeng, L., Gischkat, S., Reiche, M., Akob, D.M., Hallberg, K.B., Küsel, K., 2010. Ecophysiology of Fe-cycling bacteria in acidic sediments. *Appl. Environ. Microbiol.* 76, 8174–8183.
- Srodon, J., Drits, V.A., McCarty, D.K., Hsieh, J.C., Eberl, D.D., 2001. Quantitative X-ray diffraction analysis of clay-bearing rocks from random preparations. *Clay Clay Miner.* 49, 514–528.
- Sutton, S.R., Bertsch, P.M., Newville, M., Rivers, M., Lanzilotti, A., Eng, P., 2002. Microfluorescence and microtomography analyses of heterogeneous earth and environmental materials. *Rev. Mineral. Geochem.* 49 (1), 429–483.
- Theng, B.K.G., Orchard, V.A., 1995. Interactions of clays with microorganisms and bacterial survival in soil: a physicochemical perspective. In: Huang, P.M., Berthelin, J., Bollag, J.M., McGill, W.B., Page, A.L. (Eds.), Environmental Impact of Soil Component Interactions. Florida, CRC Press, pp. 123–139.
- Vasiliadou, I.A., Papoulis, D., Chrysikopoulos, C.V., Panagiotaras, D., Karakosta, E., Fardis, M., Papavassiliou, G., 2011. Attachment of *Pseudomonas putida* onto differently structured kaolinite minerals: a combined ATR-FTIR and 1H NMR study. *Colloids Surf. B: Biointerfaces* 84 (2), 354–359.
- Vazquez, O., Monnell, J.D., Pu, X., Neufeld, R.D., 2011. Major processes dominating the release of aluminum from smectite clays when leached with acid mine drainage. *Environ. Eng. Sci.* 28, 163–169.
- Wang, Q., Garrity, G.M., Tiedje, J.M., Cole, J.R., 2007. Naïve Bayesian classifier for rapid assignment of rRNA sequences into the new bacterial taxonomy. *Appl. Environ. Microbiol.* 73, 5261–5267.
- Waychunas, G.A., Kim, C.S., Banfield, J.F., 2005. Nanoparticulate iron oxide minerals in soils and sediments: unique properties and contaminant scavenging mechanisms. *J. Nanopart. Res.* 7, 409–433.
- Yang, Y., Colman, B.P., Bernhardt, E.S., Hochella, M.F., 2015. Importance of a nanoscience approach in the understanding of major aqueous contamination scenarios: case study from a recent coal ash spill. *Environ. Sci. Technol.* 49, 3375–3382.
- Zachara, J.M., Kukkadapu, R.K., Fredrickson, J.K., Gorby, Y.A., Smith, S.C., 2002. Biomobilization of poorly crystalline Fe (III) oxides by dissimilatory metal reducing bacteria (DMRB). *Geomicrobiol. J.* 19 (2), 179–207.